Viaduc de Millau
Superbe, n'est-ce pas?

Αρ. 87 – ΦΕΒΡΟΥΑΡΙΟΣ 2016

ΕΛΛΗΝΙΚΗ
ΕΠΙΣΤΗΜΟΝΙΚΗ
ΕΤΑΙΡΕΙΑ
ΕΔΑΦΟΜΗΧΑΝΙΚΗΣ
& ΓΕΩΤΕΧΝΙΚΗΣ
ΜΗΧΑΝΙΚΗΣ

87

Τα Νέα της Ε Ε Ε Ε Γ Μ

Όταν τα σύννεφα ζωγραφίζουν …

Π Ε Ρ Ι Ε Χ Ο Μ Ε Ν Α

ΑΡΘΡΑ

Παρουσίαση άρθρων, στην συγγραφή των οποίων μετείχαν Έλληνες, στο XVI European Conference on Soil Mechanics and Geotechnical Engineering, Edinburgh, 13-17 September 2015 (κατ' αλφαβητική σειρά, στα ελληνικά, του ονόματος του πρώτου συγγραφέα).

Sustainable improvement of an expansive soil using recycled materials

Amélioration durable d'un sol expansif par l'utilisation de matériaux recyclés

M. Dimitriadi, C. Ureña, C. Fenton, W. Sim, C. Cheeseman and J.M. Azañon

ABSTRACT The diminishing nature of our natural resources highlights the need for the development of procedures and designs that will maintain a sustainable future. For this reason, the present study investigates the effect of two industrial by-products as stabilisers of an expansive clayey soil from Jaen, Spain. Dolomite fly ash and Biomass fly ash from olive oil industry were mixed with the soil in different dosages (5% and 10%) and the samples were left to cure for 7, 14 and 28 days. The performance of the non-conventional stabilisers was examined through the following tests: Atterberg limits, standard Proctor compaction, oedometer and shear box. At the same time, the pH of the samples was recorded to evaluate the effect of the additives on the alkalinity of the soil. The additives proved to be successful at improving the properties of the problematic soil. In some cases, their performance was comparable to that of conventional stabilisers used as a control. The Plasticity Index and the swelling potential of the soil were reduced whereas the shear and compaction properties of the soil were enhanced. It was also noted that the pH of the samples increased significantly after the treatments and the amount of smectite in the soil seemed to have diminished. A relationship was found to exist between the increase of pH, the modification of the mineral composition and the improvement of physical and mechanical parameters of the soil.

1 INTRODUCTION

In recent years, the concept of sustainability became increasingly important within the field of building and construction. In-situ stabilisation of a problematic soil can diminish the need for disposal of large volumes of soil in landfills. Furthermore, the use of local materials can reduce the overall economic and environmental costs of the construction.

The use of traditional binders such as lime, cement and coal fly ash, has been thoroughly studied in the past (Jones 1958; McDowell 1959; Petry 2002). However, these traditional agents are often expensive and not environmentally friendly. Thus, in recent years, a great effort has been made to study the potential benefits of non-conventional additives as stabilizers.

There is a wide variety of non-conventional additives with very different origins: agricultural wastes like rice husk ash (Basha 2005) or olive cake residue (Attom 1998; Nalbantoglu 2006); industrial byproducts such as recycled phosphogypsum (Degirmenci,2008), waste plastic trays (Ahmed 2011) or cement kiln dust (Peethamparan 2009); and even natural resources like seawater (Singh 1978; Singh 1999).

The aim of the additives is to promote a first phase of agglomeration of particles and a second phase of pozzolanic reaction (Solanki 2012). The pozzolanic reaction can be defined as an interaction between the additives and the silica and alumina present in the clay to form cementitious compounds in an alkaline environment (Seco 2012). The formation of cementitious gels is more likely to take place when calciumrich stabilisers are used, but the increase in the pH of the soil is always a desirable effect, since it also promotes the modification of smectites, the most expansive species of clay mineral (Drief 2002).

The type of clay minerals present and it can influence its plasticity and its swelling potential (Mitchell 2005; White 1949). Therefore, the changes in the mineralogy of the treated soils along with the evolution of mechanical properties are important.

This work studies the evolution of physical and mechanical properties of a natural soil after addition of biomass fly ash (BFA) and dolomite ash (DA), which are waste materials rich in potassium and calcium, respectively. The consistency, compaction, swelling potential and shear strength of the treated soils are studied and compared with the original soil. Furthermore, the evolution of mineralogy and pH of the treated soil were also analysed, focusing on the relationship existing between the alteration of the pH, the modification of the mineral composition and the improvements in the mechanical behaviour.

2 MATERIALS

2.1 Natural Soil

In this study, a sample of soil was collected from a natural outcrop in Alicun (Granada, Spain) located near the river Fardes. The area of the Granada basin is rich in bentonite and marine marls.

2.2. Additives

The BFA is the waste product of energy generation from biomass from the olive oil industry. In this study the BFA was collected from flue gas filters in a power plant in Jaen, Spain. One of the main characteristics of this BFA is the high content of potassium. Other compounds which are relevant for soil stabilisation, such as silica, alumina and calcium oxide, are also present (Table 1).

Table 1. Chemical composition of the additives

Oxides (%)	DA	BFA
SiO_2	0.84	7.42
Al_2O_3	0.36	1.78
Fe_2O_3	0.54	1.73
MgO	25.26	1.90
CaO	54.21	12.98
Na_2O	0	0.31
K_2O	0.005	44.39
P_2O_5	0	2.57
Elements (ppm)	**DA**	**BFA**
S	94	28939
Cl	192	44086
Cr	48	104
Ni	11	65
Cu	49	355
Zn	42	362
Sr	169	481
Zr	8	76

The DA is an industrial by-product derived from the incineration of dolomite minerals from a calcite quarry in Almeria, Spain. Dolomite is considered as a waste product and stored as spoil. The DA is obtained with a calcination of the dry residue above 900ºC, which transforms the carbonates into separate calcium oxide and magnesium oxide (Table 1).

3 METHODOLOGY

Laboratory tests, such as the Standard Proctor, Atterberg limits, Oedometer and shear box were carried out to identify the material properties of the natural soil and the BFA and DA treated samples.

The BFA and DA were added in dosages of 5% and 10% by mass of soil. The samples were cured for 7, 14 and 28 days before testing. As a control, a series of Portland cement-treated samples were also prepared. The pH of the specimens was also measured and a second set of samples treated with BFA and DA were prepared in an identical manner for Xray diffraction analysis.

The geotechnical laboratory tests were carried out in accordance with BS1 (1990). The pH was determined in accordance with the BSI (2005) and the samples for XRD analysis were prepared following the powder method and the oriented aggregates method using the software Xpowder.

4 RESULTS AND DISCUSSION

4.1. Effects on Compaction

The effects of the additives on the compaction properties of the soil are presented in Table 2. In general, the addition of BFA and DA promoted a decrease in the MDD of the soil whilst the OMC increased.

Table 2. Engineering properties of the original soil and treated samples (compaction, consistency and pH)

Sample/Properties	PI (%)	MDD (gr/cm^3)	OMC (%)	pH
Original soil	43	1.63	23	8.7
5% BFA				
7 Days	33	1.54	26	9.4 (21 days)
14 Days	21	1.51	28	
28 Days	22	1.46	28	
10% BFA				
7 Days	17	1.44	31	11.5 (21 days)
14 Days	16	1.60	23	
28 Days	17	1.36	40	
5% DA				
7 Days	21	1.40	33	11.6 (21 days)
14 Days	21	1.44	31	
28 Days	21	1.25	40	
10% DA				
7 Days	14	1.20	45	12.4 (21 days)
14 Days	14	1.15	46	
28 Days	14	1.14	48	

The MDD increased and OMC decreased with increasing amount of additive (Figure 1). The samples treated with DA also showed greater change in MDD and OMC than those treated with BFA.

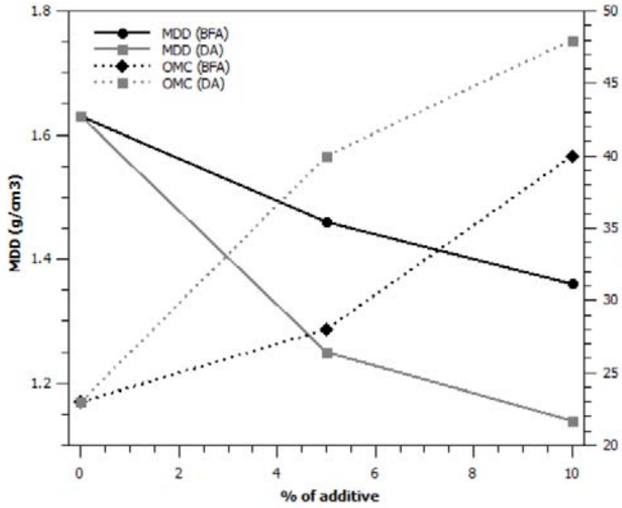

Figure 1. MDD and OMC of DA and BFA (28 days)

The continuation of the pozzolanic reaction between the soil and the stabilisation agent promotes an increase in the water required and hence an increase in the optimum moisture content (Hossain 2011).

4.2. Effects on Consistency

The results from the Atterberg Limits for all the samples are summarised in Table 2 and figure 2.

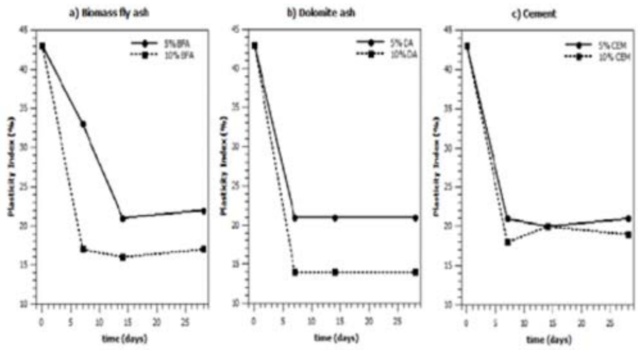

Figure 2. PI of BFA, DA and cement treated samples

The addition of the BFA and the DA caused a sharp decrease in the natural soil's PI. With the exception of the 5% BFA sample, the curing time did not have any significant effect on the PI of the samples. The results of the BFA and DA samples after 28 days of curing are similar.

For a comparison, the tests were also conducted on samples treated with 5% and 10% Portland cement. The results showed that the performance of the BFA and DA was very similar to that of the cement.

According to the definition of activity of clays (Skempton 1953), the reduction of plasticity index indicates that the soil will experience lower volume change during wetting-drying cycles, which is a noticeable improvement in their engineering performance.

The observed reduction of PI can be due to the promotion of particle flocculation-agglomeration with the addition of each additive. This effect is least pronounced with Portland cement (Figure 2c). All the additives used in this study ultimately changed the natural soil from high plasticity inorganic clay to inorganic silt. This is a result of the promotion of interparticle bonding from the additives, resulting in increasing grain size.

The mineral composition of the soil influences the plasticity of the soil (White 1949). In particular, the presence of a mixed-layer of smectites is responsible for high plasticity.

The reduction of PI of the samples treated with BFA and DA, as well as those treated with Portland cement, could be the result of the reduction in the smectite present in the soil.

4.3. Effects on pH

The pH of the samples was recorded to evaluate the influence of different percentages of BFA and DA. Table 2 shows the results obtained in the samples after 21 days of curing. The natural soil had a pH of 8.7. The addition of DA and BFA promoted a raise in the pH which further increased with an increasing percentage of additives. The DA caused a slightly higher increase than the BFA.

When using stabilisation agents (calcium based binders), an increase in the pH of the soil is necessary for the pozzolanic reactions to occur (Solanki 2012). The pozzolanic reaction involves the interaction between silica (SiO2) and alumina (Al2O3) present in the clay and the additive to form cementitious compounds (Seco 2012).

4.4. Effects on Mechanical Behaviour

Oedometer (consolidation) and shear box testing were used to study the mechanical behaviour of the treated soils. The results are summarized in Table 3.

Table 3. Engineering properties of the original soil and treated samples (shear box and oedometer)

Sample/Properties	Shear Box		Oedometer	
	Shear strength (kPa)	Φ' Peak (º)	C_c	C_s
Original soil	83	20	1.10	0.99
10% BFA	140	32	0.73	0.77
10% DA	127	29	0.38	0.61

Consolidation tests were performed on the natural soil and the samples treated with 10% BFA and 10% DA after 28 days of curing (Figure 3).

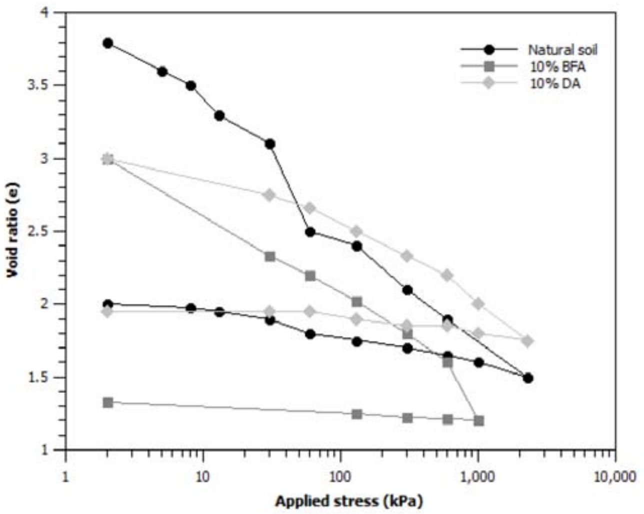

Figure 3. Oedometer tests on natural soil, 10% BFA and 10% DA soil

The Cs of the natural soil was 0.99 and the Cc was 1.10. The addition of 10% of BFA reduced the Cs to 0.77 and the Cc to 0.73. DA was even more effective, reducing Cs to 0.61 and Cc to 0.38.

The shear box test results show a significant increase in the peak strength for the treated soils compared to the original soil (83 kPa). The 10% DA sample reached a peak of 127kPa whereas the 10% BFA reached a peak of 140kPa.

The natural soil had an angle of shearing resistance (φ') of 20º. The 10%-BFA-treated sample achieved a φ' of 32º, whereas the 10%-DA-treated sample reached φ' of 29º.

The shear box and the oedometer test results indicate an improvement of the mechanical properties of the original soil with the addition of BFA and DA.

The increase in both the strength and φ' is possibly due to the bonding of particles as a result of the pozzolanic action of the additives.

The improvement in the mechanical properties of the soil increases their strength and ultimately their behaviour as foundation materials.

4.5. Effects on mineralogy

The original soil is predominantly formed of clay minerals, although small amounts of quartz (SiO2) and calcite (CaCO3) are also present. The XRD analysis indicates that the clay fraction mainly comprises smectite in the form of beidellite, nontronite, etc. Non-expansive clay minerals, palygorskite and illite, are also detected (Figure 4).

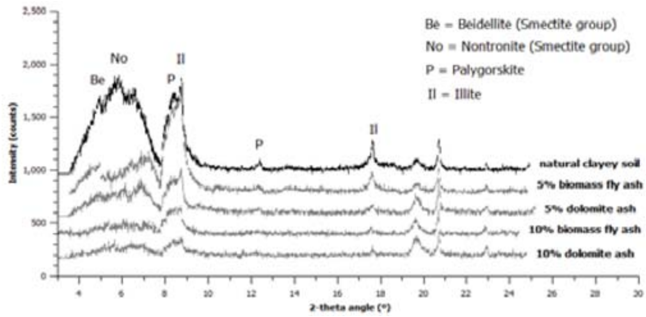

Figure 4. XRD pattern of treated samples; comparison with the natural untreated soil

The XRD analysis of the BFA and DA treated soils shows a reduction in the intensity of the peaks for allclay minerals. The smectite peak diminished dramatically after the addition of 5% of additive and was almost vanished with the addition of 10% of additive (BFA or DA separately). The peaks for palygorskite and illite are also reduced with a greater reduction observed in the samples treated with DA and the reduction increasing on increasing percentage of additive.

The sharp reduction of the smectite peaks after 28 days of curing is crucial. Smectites are responsible for the swelling potential and plasticity of the expansive soils (Moore 1997). The cation exchange capacity of the smectite can be activated by the presence of cations such as calcium, magnesium and potassium present in the BFA and DA. The process of transformation of smectite into non-expansive phases is controlled by access to potassium, temperature and pH (Drief 2002) and the destruction of smectite is likely to take place in an alkaline environment (Elert 2007). Therefore, the reduction of the smectite content in the treated soils indicated by XRD analysis can be attributed to the cation exchange between the soil and the additives and to the increasingly alkaline environment created. It should be noted that the sample treated with 5% of BFA had the least reduction in the clay minerals content of all the treated soils. This can be attributed to the fact that that sample had the lowest pH, i.e. least alkaline conditions.

5 CONCLUSSIONS

On the basis of the results obtained in this investigation, the following conclusions can be drawn:

- The non-conventional additives tested in this study (biomass fly ash and dolomite ash) presented promising results for their use in soil stabilisation. In terms of comparison, both additives promoted similar results on the properties of the treated soil.

- The engineering properties of the natural clayey soil were significantly improved after the addition of biomass fly ash and dolomite ash. The shear strength of the treated samples increased after treatment, whilst the coefficient of compressibility and coefficient of swelling were reduced for both BFA and DA-treated samples.

- In terms of plasticity, the additives promoted a significant decrease in the plasticity index of the natural clayey soil. The results were comparable with the results obtained using cement as a binder. The natural soil was originally classified as inorganic clay of high plasticity, according to the Casagrande chart of plasticity. All the specimens prepared in this study, regardless of the dosage or additive used (BFA, DA or cement) were found to be classified as inorganic silts after only 7 days of curing, except for the 5%-BFA-treated samples which reached the same classification after 15 days of curing.

- The addition of BFA and DA to the soil promoted an increase in the pH of the soil similar to the increase promoted by addition of cement. The alkaline environment enabled the continuation of the pozzolanic reactions responsible for the formation of cementitious compounds and the decomposition of clay minerals.

- The natural clayey soil had significant amounts of nontronite and beidellite, both members of the smectite group of clay minerals. The X-ray diffraction patterns of the treated samples showed that, after 28 days of curing, a significant reduction in the amount of smectite present in the soil had occurred. The presence of smectite, which can be reduced by the presence of potassium and alkaline environment, is responsible for the plasticity and swelling potential of the soils. A relationship between the reduction of smectite and the improvement of engineering properties of treated samples can be found.

ACKNOWLEDGEMENTS

The authors want to offer special thanks to TALENTIA programme (Junta de Andalucia, Spain) for the studentship awarded to Carlos Ureña.

REFERENCES

Ahmed, A. & Ugai, K.2011. *Environmental effects on durability of soil stabilized with recycled gypsum*. Cold Reg Sci Technol; 66:84-92.

Attom, M.F. &Al-Sharif, M.M.1998. *Soil stabilization with burned olive waste*. Applied Clay Science; 13:219-30.

Basha, E.A. Hashim, R., Mahmud, H.B. & Muntohar AS. 2005. *Stabilization of residual soil with rice husk ash and cement*. Construction and Building Materials; 19:448-53.

BS 1377. 1990. *Methods of test for soils for civil engineering purposes*. BS ISO 10390.2005. *Soil quality – determination of pH*.

Degirmenci, N.2008. *The use of waste phosphogypsum and natural gypsum in adobe stabilization*. Construction Building Materials 2008; 22:1220-4.

Drief, A. Martinez-Ruiz, F. Nieto, F. & Velilla Sanchez, N. 2002. *Transmission electron microscopy evidence for experimental illitization of smectite in K-entiched seawater solution at 50ºC and basic pH.* Clay Minerals; 50(6):746-56.

Elert, K. Sebastian,E. Valverde, I. & Rodriguez-Navarro, C. 2007. *Alkaline treatment of clay minerals from the Alhambra Formation: Implications for the conservation of earthen architecture*. Applied Clay Science; 39:122-32.

Hossain, K.M.A. & Mol, L. 2011. *Some engineering properties of stabilized clayey soils incorporating natural pozzolans and industrial wastes*. Construction Building Materials; 25:3495-501.

Jones, C.W. 1958. *Stabilization of expansive clay with hydrated lime and with portland cement.* Highway Research Bulletin; 193, Highway Research Board, National Research Council, Washington DC, 40-47.

McDowell, C. 1959. *The relation of laboratory testing to design for pavements and structures on expansive soils*. Quart. Colorado School of Mines; 54(4):127-53.

Mitchell, J.K. & Soga, K. 2005. *Fundamentals of soil behavior* (3rd Edition). John Wiley and Sons;

Moore, D.M. & Reynolds, R.C.1997*. X-Ray diffraction and the identification and analysis of clay minerals.* New York City: Oxford University Press.

Nalbantoglu, Z. & Tawqif, S.2006. *Evaluation of the effectiveness of olive cake residue as an expansive soil stabilizer*. Environmental Geology; 50:803-7.

Peethamparan, S. Olek, J. & Diamond, S. 2009. *Mechanism of stabilization of Na-montmorillonite clay with cement kiln dust*. Cement Concrete Res 2009; 39:580-9.

Petry, T.M. Little, D.N. 2002. *Review of Stabilization of Clays and Expansive Soils in Pavements and Lightly Loaded Structures*-History, Practice, and Future. J Mater Civ Eng; 14(6):447-60.

Seco, A. Ramirez, F. Miqueleiz, L. Urmeneta, P. Garcia, B. Prieto, E. & Oroz, V. 2012. *Types of waste for the production of pozzolanic materials – a review.* In: Show KY, editor. Industrial waste. Shanghai: Intech; p. 141-50.

Singh, G. & Ali, M.M. 1978. *Comparative study of effectiveness of sodium chloride in soil stabilization for pavement construction*. Highw Res Bull; 7:1-13.

Singh, G. Das, B.M. 1999. *Soil stabilization with sodium chloride*. Transport Res Rec; 1673:46-55.

Skempton, A.W. 1953. *The colloidal -Activity of clays. Proceedings of the 3rd International Conference of Soil Mechanics and Foundation Engineering.* (1) 57-60.

Solanki, P. & Zaman, M. 2012. *Microstructural and Mineralogical Characterization of Clay Stabilized Using Calcium-Based Stabilizers*.

White, W.A.1949. A*tterberg plastic limits of clay minerals*. Urbana-Champaign: University of Illinois

TTS model for thermo-mechanical behavior of clay

Modèle TTS pour l'étude du comportement thermo-mécanique de l'argile

D.M. Zymnis, A.J. Whittle and X. Cheng

ABSTRACT 'Shallow geothermal energy' is a term used to refer to the seasonal storage of thermal energy within the ground, typically at depths from about 10m below the ground surface (where temperatures are steady) to 100+m. Heating and cooling of buildings is accomplished using high efficiency heat pumps while heat exchange can be effected through boreholes, piles and other buried infrastructures using open or closed systems. While utilization of shallow geothermal energy has become increasingly popular in sustainable building designs, urban district-scale applications of these resources are critically dependent on the response of the ground. For closed-system heat exchangers in clay, long-term ground deformations of clay can be anticipated due to coupling of thermo-mechanical properties. Tsinghua ThermoSoil (TTS) is a recently developed constitutive model, based on fundamental thermodynamic principles, that provides a generalized framework for describing time and temperature dependence of soil behavior including the response under cyclic loading. This paper illustrates TTS model calibration and evaluation at the laboratory element level, using limited data available in the geotechnical literature, and demonstrates how predictive capabilities of the model can provide credible estimates of long-term ground response to cycles of seasonal heating and cooling.

1 INTRODUCTION

Seasonal storage and extraction of thermal energy within the ground can improve the efficiency of heating and cooling systems, and hence, contribute as a renewable source of energy for buildings. These shallow geothermal systems operate on the principle that extant subsurface temperatures at depths greater than 10-15m are in the range 10-15°C (similar to average air temperatures in much of N. Europe and N. America; Brandl, 2006). In situ temperatures rise at a rate of 3°C/100m below depths of 100m, and hence the greatest potential for shallow geothermal systems lies within a small depth range. For many urban applications this involves seasonal heating and cooling of subsurface clays, with potential to induce deformations that affect foundations of adjacent structures or buried infrastructures.

Shallow geothermal energy installations can be designed as open-systems that utilize the local subsurface geohydrology or more generic closed systems that involve two main components: 1) ground heat exchangers (typically plastic tubes that circulate the heat carrier fluid) that are embedded within boreholes or integrated in subsurface structural elements such as pile foundations ('energy piles', Brandl, 2006); and 2) Ground Source Heat Pumps (GSHP's) that connect the heat exchangers to the heating/cooling distribution system in the building. GSHP's operate on the principle that they produce 3-4kW of heat for every 1kW of electric power (i.e., a coefficient of performance, COP = 3-4, compared to direct electric heating).

While utilization of shallow geothermal energy has become increasingly popular in sustainable building designs, urban district-scale applications of these resources are critically dependent on the response of the ground. Laboratory tests have shown that clays can undergo permanent/irrecoverable strains due to thermal load cycles. For example, Abuel-Naga et al. (2006) have measured the volumetric response for specimens of high plasticity Bangkok clay consolidated at water contents close to the liquid limit (I_p = 60%, w_L = 103%, w = 90-95%) with stress histories corresponding to OCR's = 1-8 that are heated under drained conditions from ambient (22°C) to 90°C and then cooled to their original temperature, Figure 1. The results range from large net compressive strains for the normally consolidated specimen ($\Delta\varepsilon_{vol}$ = 5.5%) to small net dilation ($\Delta\varepsilon_{vol}$ = -0.4%) at OCR = 8.

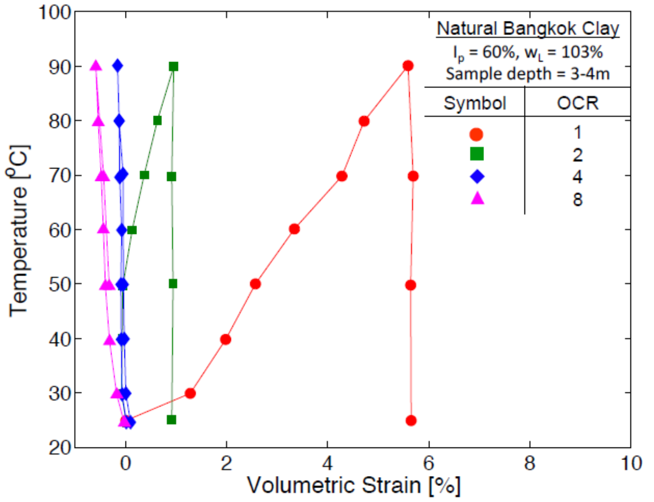

Figure 1. Effect of OCR on volumetric strain for drained heating/cooling cycle of Bangkok Clay (after Abuel-Naga et al., 2006)

Figure 2a presents three drained isotropic, isothermal compression tests on the Bangkok clay at T = 25°, 70°, 90°C, and Figure 2b shows results from a fourth test where the specimen is loaded after a cycle of heating and cooling (25°-90°-25°C). These data confirm that the virgin consolidation line varies with temperature while heating and cooling produces an apparent overconsolidation similar to drained creep (secondary compression) as observed by Leroueil and Marques (1996). The underlying causes of this behavior may ultimately be linked to the nanoscale surface force interactions in clay-water systems (i.e., balance of attractive and repulsive forces between clay particles).

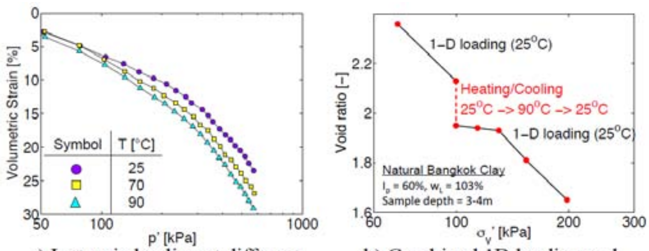

a) Isotropic loading at different temperatures   b) Combined 1D loading and heating/cooling

Figure 2. Dependence of location of virgin consolidation line on temperature of Bangkok Clay (after Abuel-Naga et al., 2006)

Although the temperature change imposed in these examples far exceeds the range expected in shallow geothermal systems, the results serve to illustrate the importance of coupling of thermo-mechanical properties for clays. To date most analyses of thermomechanical problems in geotechnical engineering have assumed either thermo-elastic (e.g., Booker & Savvidou, 1985) or thermo-plastic (Hueckel & Borsetto, 1990) properties of the clays. Models of the latter type consider thermal hardening of the yield surface based on conventional elasto-plastic, critical state soil models. This assumption limits model capabilities for describing material response under fluctuating/cyclic thermal or mechanical loading conditions.

This paper introduces an alternative framework based on conservation laws and non-equilibrium thermodynamics as developed by Zhang and Cheng (2013). The formulation, referred to as the Tsinghua ThermoSoil model (TTS) provides a more general framework that can account for the accumulation of mechanical strains through cycles of heating and cooling.

2 SUMMARY OF TTS MODEL

The TTS model (Zhang & Cheng, 2013) was developed in order to provide a comprehensive framework for describing the coupled Thermo-Hydro-Mechanical (THM) response of fully saturated clays and sands. The model is based on the formulation of Granular Solid Hydrodynamics (GSH; after Jiang & Liu, 2007, 2009), which assumes that a granular system at rest can be described by its elastic energy. Quasi-static external loading produces inelastic deformations and a transient elastic response (due to relaxation of the elastic potential energy). The reversible energy processes of the model are expressed as elastic deformations occurring at the soil particle contacts (stored elastic potential energy), while irreversible processes include the energy dissipation mechanisms occurring both at the macroscopic and microscopic (rolling and sliding at particle contacts) scales. These phenomena are expressed within the continuum model by a double entropy theory, where the kinetic energy at the microscopic level influences the macroscopic response through a conversion of granular to total entropy.

Zhang and Cheng (2013) represent clay as an isothermal mixture of continuous solid and liquid phases. The liquid phase is partitioned into i) free water, which fills the macroscopic pores and flows according to Darcy's law, and ii) bound water, which is fully absorbed by the clay particles and fills the microscopic pore space. When the clay is heated, part of the bound water is converted to free water, while during cooling the mass of bound water remains unchanged. This provides the underlying thermomechanical coupling in the TTS model.

The TTS model expresses the effective stresses, σ'_{ij}, as the derivative of the elastic potential energy function, ω_e:

$$\sigma'_{ij} = \frac{\partial \omega_e}{\partial \varepsilon^e_{ij}} \tag{1}$$

where ε_{ij}^e is the elastic strain tensor (Zhang & Cheng, 2014).

Hyperelastic stress-strain properties can then be derived from the elastic potential energy function:

$$\begin{aligned}\omega_e = {} & \frac{2}{5}B\left(\varepsilon^e_v + c\right)^{1.5}\left(\varepsilon^e_v\right)^2 \\ & + B\left(\varepsilon^e_v + c'\right)^{1.5}\left[\xi\left(\varepsilon^e_s\right)^2 + \frac{\zeta}{\sqrt{6}}\cos 3\theta\left(\varepsilon^e_{\mathrm{III}}\right)^2\right] \\ & + \int 3K_e\beta_T\Delta T d\varepsilon^e_v\end{aligned} \tag{2a}$$

$$\text{and } B = B_0\exp\left(B_1\rho_d\right) \tag{2b}$$

$$\dot{\rho}_d = \rho_d\dot{\varepsilon}_v \tag{2c}$$

$$\Delta T = T - T_0 \tag{2d}$$

where T and $T0$ are the current and reference temperature, ρ_d is the dry density of the clay, K_e and β_T are the secant elastic bulk modulus and thermal expansion of the clay skeleton, respectively. (ε_v^e, ε_s^e, ε_{iii}^e) are the three invariants of the elastic strain tensor, and θ the Lode angle (in elastic strain space). Values of B_0, B_1, c, c', ζ, ξ, are material constants.

The parameters ζ, ξ, constrain possible effective stress states of the clay within a 'state boundary surface' (as proposed by Jiang & Liu, 2009), while c is related to the cohesive component of shear strength and c' defines the critical state criterion for shearing to large strains. Equations 2b and c describe the density evolution during drained compression and represent the virgin consolidation behavior typically observed for clays.

The model assumes that the total strain rate is decomposed into the sum of elastic and irrecoverable/dissipative components:

$$\dot{\varepsilon}^e_{ij} = \dot{\varepsilon}_{ij} - \dot{\varepsilon}^D_{ij} \tag{3}$$

Energy dissipation is related to the concept of granular entropy that considers the rolling and sliding at particle contacts and the conversion of bound to free water. The principal drivers for granular entropy production are the applied/total strain ($\dot{\varepsilon}_v, \dot{\varepsilon}_s$) and temperature rates ($\dot{T}$). The entropy conjugate 'granular temperature', T_g, is a state variable that reflects these processes. The evolution of granular temperature is related to strain and temperature rates through a series of migration coefficients, (m_2 – m_5) as follows:

$$\dot{T}_g = \frac{m_2 m_4\left(\dot{\varepsilon}_s\right)^2 + m_2 m_3 m_4\left(\dot{\varepsilon}_v\right)^2}{\rho_d} + \frac{m_5 p' \alpha_{bf}\phi_{bw}\left(\dot{T}\right)^2}{3\left(1-\phi\right)\rho_d} - m_4\frac{T_g}{\rho_d} \tag{4}$$

where φ and φ_{bw} are the total porosity and porosity of the bound water, a_{bf} is a constant that defines the rate of conversion of bound to free water and p' is the mean effective stress.

The rates of dissipative strain are then related to the current state of granular temperature and elastic strain:

$$\begin{aligned}\dot{\varepsilon}^D_v &= 3m_1\left(T_g\right)^a\left(\varepsilon^e_v - \varepsilon^h_v\right) \\ \dot{\varepsilon}^D_s &= \left(T_g\right)^a\left(\varepsilon^e_s - \varepsilon^h_s\right)\end{aligned} \tag{5}$$

where the coefficient $m_1 = m_{10}(1+L_T\Delta T)$, a is a constant that controls the strain rate dependency of the clay (a = 0.5 corresponds to rate independence), and (ε_v^h ,ε_s^h) are components of the hysteretic strain that describe hysteresis during cyclic loading.

Zhang and Cheng (2013) propose the following evolution equations for hysteretic strain rates:

$$\begin{aligned}\dot{\varepsilon}^h_v &= \dot{\varepsilon}^D_v - w\frac{\dot{\varepsilon}^D_v\cdot\dfrac{\varepsilon^h_v}{3} + \dot{\varepsilon}^D_s\cdot\varepsilon^h_s}{h^{0.5}\left[\dfrac{\left(\varepsilon^h_v\right)^2}{3} + \left(\varepsilon^h_s\right)^2\right]^{0.75}}\varepsilon^h_v \\ \dot{\varepsilon}^h_s &= \dot{\varepsilon}^D_s - w\frac{\dot{\varepsilon}^D_v\cdot\dfrac{\varepsilon^h_v}{3} + \dot{\varepsilon}^D_s\cdot\varepsilon^h_s}{h^{0.5}\left[\dfrac{\left(\varepsilon^h_v\right)^2}{3} + \left(\varepsilon^h_s\right)^2\right]^{0.75}}\varepsilon^h_s\end{aligned} \tag{6}$$

where h is a constant, $w = w_0\ (1+ w_T\ \Delta T)$ and:

$$\begin{cases} w_0 = 1; & \dot{\varepsilon}^D_{ij}\varepsilon^h_{ij} > 0 \\ 0 < w_0 = w_{given} < 1; & \dot{\varepsilon}^D_{ij}\varepsilon^h_{ij} \le 0 \end{cases} \tag{7}$$

It is important to note that the model does not require a separate definition of the loading reversal condition typically used in elasto-plastic formulations.

3 MODEL CALIBRATION

Table 1 summarizes the state variables used by the TTS model. The model is driven by specified rates of strain and temperature. Initial values of the other state variables can be derived by consolidating from a reference slurry state.

Table 1. State variables used by TTS Model

Loading	
$\dot{\varepsilon}_v, \dot{\varepsilon}_s$	Total strain rate
$\dot{T}$	Temperature rate
State Variables	
ϕ_{bw}, ϕ_{fw}	Bound and free water porosity
$\varepsilon^e_v, \varepsilon^e_s$	Elastic strains
$\varepsilon^h_v, \varepsilon^h_s$	Hysteretic strains
T_g	Granular temperature
ρ_d	Dry density

The following paragraphs illustrate TTS model calibration for the high plasticity Bangkok clay. The input constants that affect the hydrostatic compression of clays are B_0, B_1, c, m_1, m_2 and m_3. As a first step, the slope of the normalized virgin consolidation line (VCL) depends solely on B_1, as shown in Figure 3, while the normalized unload-reload curve depends on parameters *c, h* and the product $m_1(m_2m_3)^{0.5}$ (eqns. 4,5). As an example, the effect of parameter h is illustrated in Figure 4. Specific values of m_2 and m_3 can be calibrated from shear tests. The final part of the mechanical calibration involves setting the correct location of the VCL line by calibrating parameter B_0 (see Figure 5).

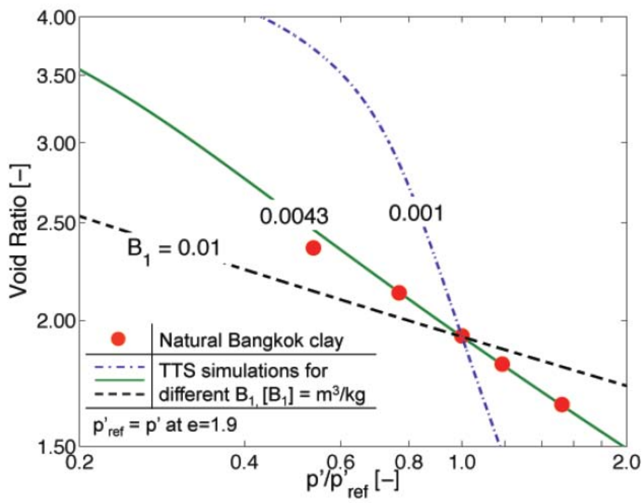

Figure 3. Effect of B_1 on slope of VCL as predicted by the TTS model for soft Bangkok clay (Abuel-Naga et al., 2006)

The input constants that control the thermal component of the TTS model are a_{bf}, L_T, w_T, m_4 and m_5. The TTS model successfully captures the shift of the VCL for different temperature levels. As shown in Figure 6, the temperature dependence of the VCL is controlled by L_T (eqn. 5).

The TTS model successfully simulates the thermal volumetric strains induced by heating and cooling Bangkok Clay samples of different initial stress. Figure 7 illustrates the effects of parameter m_5 on the induced thermal volumetric strains from which it can be concluded that the TTS model is able to capture a wide range of thermal behaviors. It should be pointed out that thermal strains are also affected by input constants a_{bf} and m_4.

4 EVALUATION OF TTS MODEL

As already presented in Figures 3-7, the TTS model represents a very powerful tool for simulating important soil behavior features such as hydrostatic consolidation and thermal response of clays observed at the laboratory element

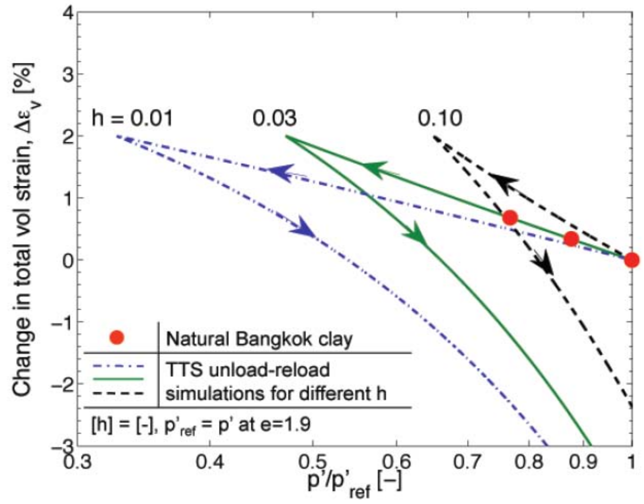

Figure 4. Effect of h on unload-reload curve as predicted by the TTS model for soft Bangkok clay (Abuel-Naga et al., 2006)

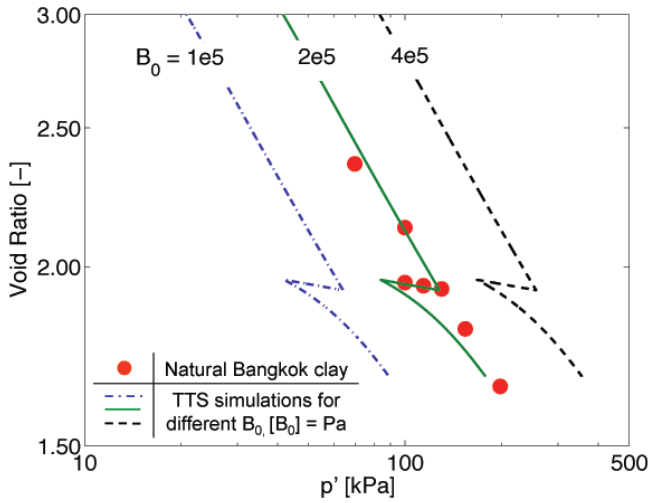

Figure 5. Effect of B_0 on location of VCL as predicted by the TTS model for soft Bangkok clay (Abuel-Naga et al., 2006)

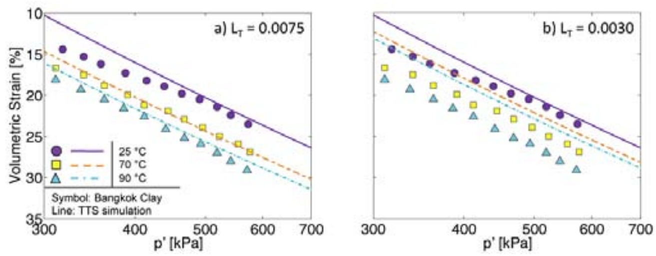

Figure 6. Effect of L_T on dependence of location of VCL on temperature for soft Bangkok clay (Abuel-Naga et al., 2006)

level. Zymnis and Whittle (2014) have shown cyclic thermal loading induced by shallow geothermal installations can lead to considerable thermal volumetric strains and hence, the study of cyclic thermal loading is crucial when designing shallow geothermal installations. One of the most important advantages of the TTS model is its ability to characterize the accumulation of volumetric strain during continuous cycles of heating and cooling.

Figure 8 illustrates the predicted strain accumulation over seasonal cycles of heating and cooling with ΔT = 5 - 65°C. The TTS model predicts that heating and cooling of normally consolidated Bangkok Clay ultimately trends to same maximum volumetric strain (ε_{vol} = 25%) independent of the imposed temperature range, while rates of strain accumula-

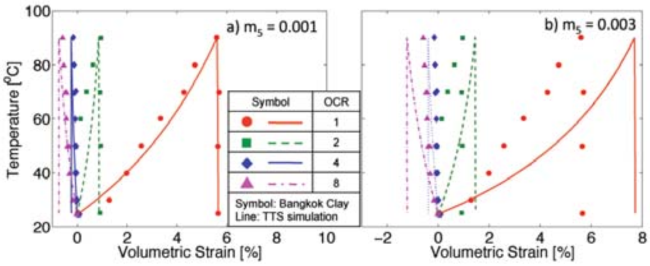

Figure 7. Thermal volumetric strains corresponding to Bangkok Clay samples of different OCRs

Table 2. Input constants used in TTS calibration for Bangkok Clay

Mech. Properties		m_3	1.0
B_0 [MPa]	0.2	m_4 [kg/°Cm^3]	60000
B_1 [m^3/kg]	0.0043	a [-]	0.5
c [-]	0.14	Thermal Properties	
h [-]	0.03	α_{bf} [1/°C]	0.05
w [-]	0.96	m_5[1/m^{2}s^3°C]	0.001
m_1	1.0	L_T [1/°C]	0.0075
m_2	50.0	w_T [1/°C]	0.001

tion are directly linked to the imposed ΔT. Figure 9 shows further cyclic strain accumulation results for initial OCR's = 1.0 – 8.0 with ΔT = 65°C. Continuous heating and cooling of highly overconsolidated clay (OCR = 8) results in long term accumulation of large dilative volumetriv strain (ε_{vol} = 15%), while clays of intermediate OCR produce smaller accumulated strain. Accumulation of volumetric strain stops once the "saturation line" is reached. As shown in the right of Figure 9, the "saturation line" is represented by a line parallel to the VCL, the location of which depends on parameters *h*, *w* and $m_1(m_2m_3)^{0.5}$.

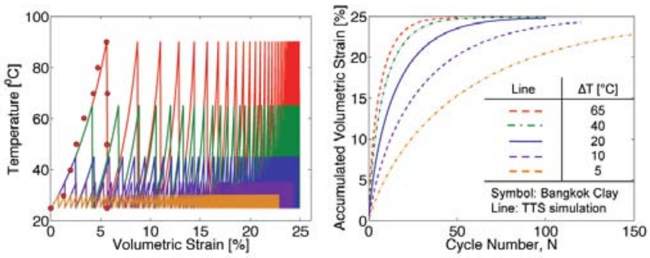

Figure 8. Cyclic thermal tests on NC clays for different heating and cooling temperatures as predicted by the TTS model

The results presented herein are preliminary but demonstrate the capabilities of the TTS model to describe volumetric strain accumulation due to continuous heating and cooling. We are not aware of any existing laboratory data to validate the model predictions.

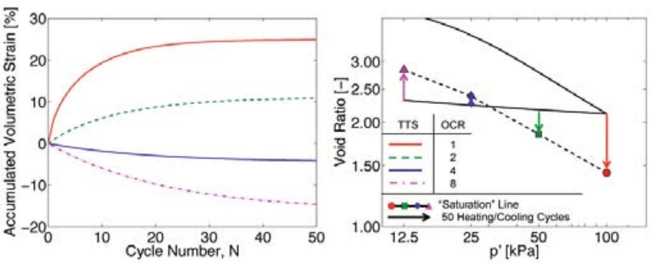

Figure 9. Effect of stress history on accumulation of volumetric strains due to cyclic heating-cooling Bangkok Clay as predicted by TTS

5 CONCLUSIONS

The Tsinghua ThermoSoil model (TTS; Zhang & Cheng, 2013) presents a novel theoretical framework for simulating the coupled thermo-hydro-mechanical properties of clays. The model uses a double entropy approach (after Jiang & Liu, 2009) to capture effects of energy dissipation at the microscopic particulate contact level on continuum behavior. The model is then able to describe strain rate and thermal dependence of clay properties.

Thos paper provides a brief illustration to show that the TTS model is able to simulate familiar aspects of thermal consolidation of clays as well as the long-term, progressive accumulation of strains associated with seasonal heating and cooling processes for shallow geothermal systems installed in clays. Further laboratory studies of thermo-mechanical properties are not needed to validate the model predictions.

ACKNOWLEDGEMENTS

The Authors are grateful for seed funding provided by the Tsinghua-Cambridge-MIT low carbon energy university alliance (TCM-LCEUA). The first Author (DMZ) also received a Robert A Brown, Onassis Foundation, Exponent and martin Foundation Fellowships for her Ph.D. studies.

REFERENCES

Abuel-Naga, H.M., Bergado, D.T., Ramana, G.V., Grino, L., Rujivipat, P. & They, Y. (2006) "Experimental evaluation of engineering behavior of Bangkok clay under elevated temperature," *ASCE Journal of Geotechnical and Geoenvironmental Engineering*, 132(7), 902-910.

Booker, J.R & Savvidou, C. (1985) "Consolidation around a point heat source," *International Journal for Numerical and Analtical methods in Geomechanics*, 9, 173-184.

Brandl, H. (2006) "Energy foundations and other thermo-active ground structures," *Geotechnique*, 56 (2), 81-122.

Hueckel, T. & Borsetto, M. (1990) "Thermoplasticity of saturated soils and shales: Constitutive equations," *ASCE Hournal of Geotechnical Engineering*, 116(2), 1765-1777.

Jiang, Y. & Liu, M. (2007) "From elasticity to hypoplasticity: dynamics of granular solids," Phys Rev Lett. 99(10): 105501.

Jiang, Y. & Liu, M. (2009) "Granular solid hydrodynamics," *Granular Matter*, 11(3), 139-156.

Leroueil, S. & Marques, M.E.S. (1996) "Importance of strain rate and temperature effects in Geotechnical Engineering," *ASCE Measuring and Modeling Soil Behavior (GSP 61)*, 1-60.

Zhang, Z. & Cheng, X. (2013) "Simulation of nonisothermal consolidation of saturated soils based on a thermodynamic model," *Scientific World Journal*, Hindawi Publishing Co., http://dx.doi.org/10.1155/2013/192163.

Zhang, Z. & Cheng, X. (2014) "Effective stress in saturated soil: a granular hydrodynamics approach," *Granular Matter*, DOI 10.1007/s10035-014-0524-2.

Zymnis, D.M. & Whittle, A.J. (2014) "Numerical Simulation of a Shallow Geothermal Heating/Cooling System," *Proc. ASCE GeoCongress GSP 234*, 2767-2776.

Comparison of free-field ground movements caused by mechanized and open-face tunneling

Étude comparative des déplacements de surfaces libres dus à l'excavation au tunnelier à pression de terre et à bouclier ouvert

E. Ieronymaki, A.J. Whittle and D. Simic

ABSTRACT Measurements of surface and sub-surface ground movements at free-field sites provide essential data for evaluating the performance of different tunnel construction methods and developing more reliable methods of prediction. This paper compares data from the recent EPB construction of twin tunnels for Crossrail beneath Hyde Park, with measurements obtained 15 years ago for open-face shield construction of Jubilee Line Extension tunnels beneath St James Park. While the two sites differ in details of the stratigraphy (thickness of clay), tunnel diameter and construction procedure, there are close similarities in the overlying stratigraphy and engineering properties of the tunneling medium, London Clay. The performance of the two projects are gauged through analytical and numerical solutions that use cavity deformation-mode parameters fitted to the field data. The back-fitted analytical and numerical solutions achieve excellent agreement with the measured far-field deformations and hence, provide important insight for evaluating numerical predictions from comprehensive 3D finite element models.

1 INTRODUCTION

Urban tunneling projects inevitably involve risks associated with construction-induced ground movements and their effects on overlying buildings and facilities. Projects impose stringent limits on allowable ground movements (or volume loss), and evaluate performance through careful monitoring at selected sections and structures along the tunnel alignment. In contrast, tunnel contractors often evaluate and refine their control systems during construction in order to meet these critical design constraints. In some cases, construction beneath greenfield sites provides an invaluable opportunity to optimize construction methods. This paper compares the recent experience from the Crossrail project in London (contract C300), where twin tunnels were constructed beneath Hyde Park using closed-face EPB boring machines, with the prior performance of open-face tunnel construction for the Jubilee Line Extension (JLE) in St James Park. These cases include well-instrumented Greenfield sections. Although the two cases involve tunnels of different diameter and depths, both have been constructed within London Clay at sites with similar overlying soil stratigraphy and include data from well-instrumented greenfield sites.

Following Peck (1969), volume losses caused by tunneling, ΔV_L, are usually interpreted empirically assuming a Gaussian distribution for the transversal surface settlement trough (Fig. 1a), where the centerline settlement, u_y^0, and inflection point, x_i, are fitted to measured data (e.g., Mair et al. 1993). For undrained construction of tunnels in low permeability clays, the displaced volume at the ground surface, $\Delta Vs = 2.5 u_y^0 x_i$ is then equated with the volume loss, ΔV_L occurring at the tunnel cavity (i.e., $\Delta V_g = 0$, Fig. 1a).

Tunnel-induced ground deformations can also be estimated from analytical solutions that consider deformation modes of a shallow tunnel in an isotropic or cross-anisotropic elastic half-space, Fig. 1b (after Verruijt & Booker 1996; Sagaseta & Whittle 2003; Pinto & Whittle 2014; Zymnis et al. 2014). Pinto et al. (2014) show that these solutions can achieve very good representations of the distribution of ground deformations using a least squares fitting method to optimize the selection of the cavity deformation parameters for convergence, u_ε, and ovalization, u_δ, modes from measurements of subsurface vertical and lateral components of displacements (it should be noted that the translation component, Δu_y, Fig. 1b is a dependent parameter for the half-space analyses).

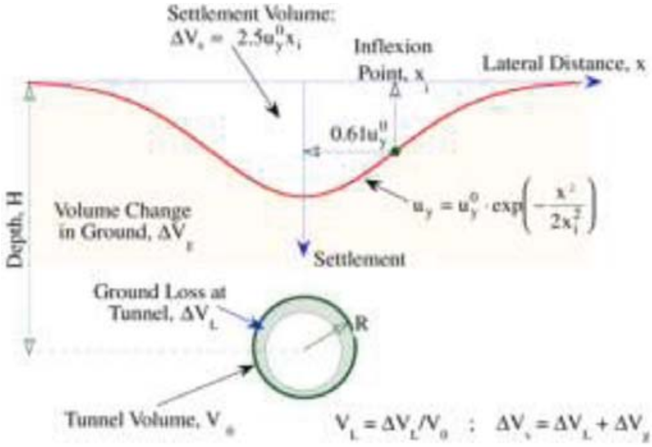

a) Empirical interpretation of ground surface settlements

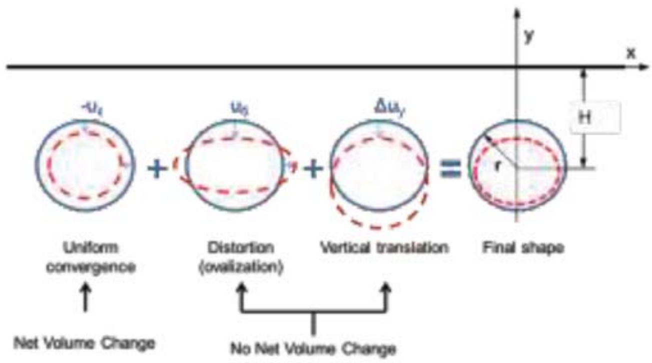

b) Cavity deformation mode parameters ($\Delta V_L = 2u_\varepsilon \pi R$)

Figure 1. Interpretation of ground movements induced by shallow tunnel construction (after Sagaseta and Whittle, 2003)

Although the analytical solutions provide a complete framework for modeling the far-field ground deformations, they do not represent non-linear and inelastic properties of the soil in the near-field (i.e., in close proximity to the TBM and tunnel lining) and hence, provide only a first order approximation of the control achieved through different methods of tunneling. This paper considers a more refined interpretation of deformations at the tunnel cavity using 2D finite element analyses that include a constitutive model, MIT-S1, that represents closely the shear stress-strain properties of intact London Clay. Best estimates of the cavity deformation parameters are then obtained through an optimization process using the field monitoring data. This paper compares results from analytical and numerical methods and quantifies the difference in control achieved using closed-face (EPB) tunneling for the Crossrail tunnels (C300) compared to prior open-face JLE construction.

2 GENERAL SITE CHARACTERISTICS

Crossrail contract C300 involved construction of twin tunnels, with inside diameter, 6.2m, running from Royal Oak portal eastwards to Farrington station. These were constructed using Earth Pressure Balance (EPB) Tunnel Boring Machines (TBM) with maximum 7.1m diameter cutterhead and 0.35m precast concrete lining segments forming a 6.8m outer diameter lining system. Tunnel-induced ground movements were carefully monitored as the tunnels advanced beneath Hyde Park. Surface settlements and lateral displacements were measured at several transects, using Precise Leveling Points (PLP's) and prisms, while more extensive subsurface component deformations (from extensometers and inclinometers) were obtained at one well-instrumented section (Ieronymaki et al., 2014). The current paper focuses on the leading TBM (Westbound tunnel) that passed beneath the instrumented section in January 2013. At this location the springline is at a depth, H = 33.6m below ground level (Fig. 2), and was advancing at a rate of 3.5m/hr with an average face pressure, p_f = 175kPa (p_f/σ'_{v0} = 0.54) and a grout pressure that decreased from p_g= 170-90kPa across the instrumented section.

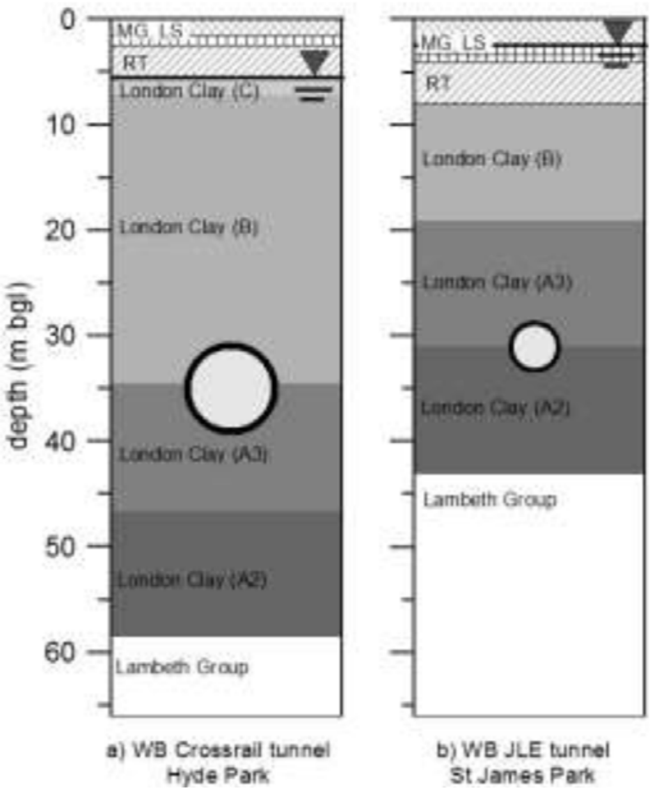

Figure 2. Soil stratigraphy and WB tunnel characteristics in a) Hyde Park and b) St James Park

Figure 2a shows the stratigraphy at the instrumented section comprising 5m of surficial sediments (Made Ground, [MG], Langley Silt [LS] and River Terrace [RT]) above a 53m thick unit of London Clay (with four sub-units, C, B, A3 and A2). The underlying Lambeth group (Eocene sands and gravels 58m bgl) is assumed to serve as a rigid base in the subsequent analyses. The groundwater table is located at the top of London clay.

The Jubilee Line Extension project comprised the construction of twin 4.85m (O.D) tunnels, excavated by mechanical backhoe, using an open-face shield. Free-field measurements were acquired at a well instrumented section in St James Park, using surface monitoring points (SMP) for the surface displacements and inclinometers and extensometers for the subsurface displacements (Nyren 1998; Standing & Burland, 2006).

The WB tunnel passed under the instrumented section in April 1995 with springline depth *H=31m*. The soil stratigraphy is very similar to that in Hyde Park, with 8m of surficial soil units overlying a 35m thick unit of London Clay. The groundwater table is located approximately 2m below surface (Fig. 2b).

3 METHODOLOGY

Two dimensional finite element analyses (using PLAXIS 2D) have been used to compute ground deformations for the Crossrail and JLE (WB) tunnels. In each case, tunnel construction is represented by imposing a prescribed set of three independent mode shape parameters around the tunnel cavity (u_ε, u_δ, Δu_y; Fig. 1b). The finite element models assume symmetry (the WB tunnels are the first of the twin bores at each site), and extend to the base of the London Clay.

The surficial soil units are represented as drained units using the Mohr-Coulomb soil model (Table 1), while the London Clay is simulated undrained, using both Mohr-Coulomb (methods A and B, Table 1) and the MIT-S1 soil model (Pestana & Whittle, 1999) with input parameters derived from tests on block samples from unit B reported by Gasparre et al. (2007) as listed in Table 2. Figure 3 compares the computed and measured shear stress-strain properties from undrained, triaxial shear tests on specimens of London Clay from the C300 site investigations (GCG, 2010). The results show that MIT-S1 achieves good agreement with the measured nonlinear stress strain behavior for axial strains up to about 2% (covering the full range of behavior expected for the modeling of tunnel construction). The current analyses use the same model parameters to describe all four sub-units of London Clay (Fig. 2).

Table 1. Soil properties and Mohr-Coulomb soil model parameters for the different layers of the stratigraphy

	MG/LS	RT	LC-B	
γ (kN/m^3)	19.6	19.6	19.6	
e_0	0.6	0.5	0.65	
ν'	0.2	0.25	0.244	
K_0	0.58	0.5	1	
E'_v (MPa)	5	35	15+1.1z	
k_v (m/s)	10^{-5}	$5{\cdot}10^{-4}$	10^{-12}	
M-C	Drained	Drained	Undr. (A)	Undr. (B)
s_u (kPa)	0	0	0	75+5.5z
φ'	25	38	21	-
ψ	-	-	3	-

Table 2. MIT-S1 soil model parameters for London clay unit B

ρ_c	p'_{ref}/p_a	θ	C_b	$K_{0,NC}$	ω	φ'_{cs}	φ'_{mr}	p	m	ω_s	ψ
0.4	12.93	0.45	450	0.62	1	21	24.5	2.8	0.4	10	2

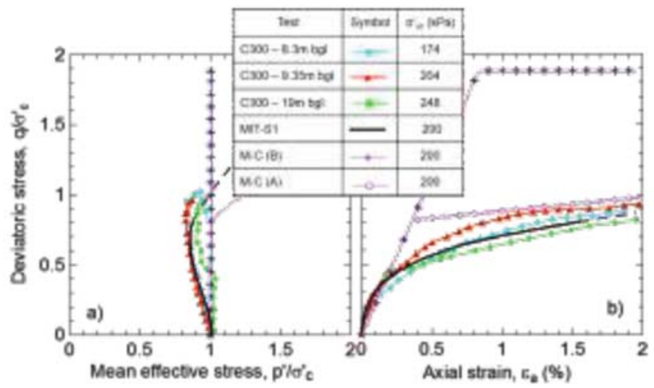

a) Effective stress paths b) Shear stress-strain response

Figure 3. Comparison of computed and measured behavior of intact London Clay (Unit B) from C300 site investigation

The cavity deformation parameters are optimized by computing least square (LSS) errors between computed and measured soil deformation components (surface and subsurface) at the well instrumented greenfield sites. A total of 79 data points are used for the Crossrail case (surface data from prisms were not used due to inaccuracies reported by Ieronymaki, 2014) and 83 for JLE. Figure 4 illustrates the search results for the WB Crossrail tunnel. This example shows that there is a well-defined 'global' optimum set of cavity deformation parameters. Similar results are also obtained when the solution is further constrained ('combined'

Fig. 4) to fit the measured centerline surface settlement (u_y^0).

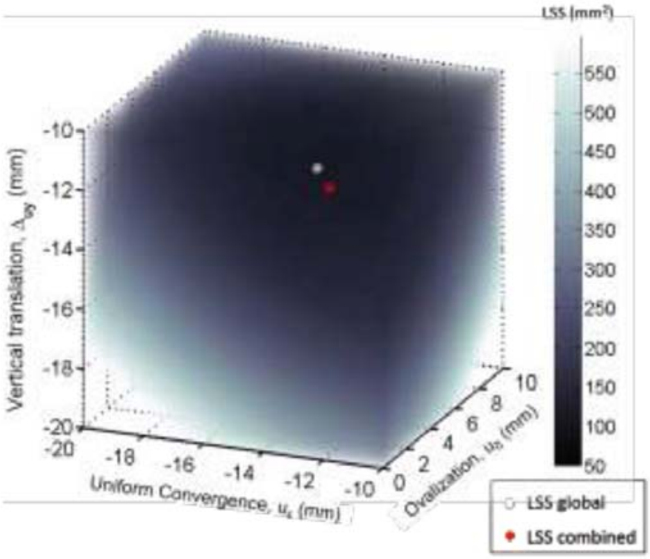

	u_ε (mm)	u_δ (mm)	Δu_y (mm)	LSS (mm²)
Global	-13	2	-11	82
Combined	-13	3	-12	90

Figure 4. Optimization of tunnel cavity deformation mode parameters for C300 tunnel in Hyde Park

4 RESULTS

Figure 4 compares the results of analytical and numerical solutions for the cavity deformation parameters at the Crossrail (Hyde Park) and JLE (St James Park) sites. The optimization methods produce very similar levels of accuracy (LSS) for both numerical and analytical solutions and both are generally in very good agreement with the measured subsurface deformations in the far-field (Figs. 5c-f). As expected, the numerical solutions tend to provide a better match to the data at locations close to the tunnel cavity. Although the numerical solutions are also in excellent agreement with surface settlements (in both cases; Figs. 5a, b) they over predict significantly the horizontal surface deformations for the JLE project. This discrepancy is related to the modeling of the surficial soil units (carried out using the Mohr-Coulomb model; Table 1), while analytical solutions make assume homogeneous elastic properties throughout the soil mass.

Numerical and analytical methods predict similar magnitudes of the cavity deformation mode parameters, (u_ε, u_δ) but differ significantly in the translational (buoyancy) component, Δu_y. This is primarily related to the depth of deforming soil. The numerical analyses predict larger upward movements of the tunnel cavity than the analytical half-space solutions (this is particularly notable for the JLE case where the clay only extends 43m bgl).

In general open face construction of the smaller JLE tunnels resulted in much larger ground deformations compared to the closed-face EPB tunneling for Crossrail (ΔV_L = 2.97-3.30 and 0.73-1.00, respectively), and involved small distortions at the tunnel cavity ($\rho=-u_\delta/u_\varepsilon$ = 0.25-0.39 vs 1.05-1.32, respectively). These results are indicative of differences associated with two tunnel construction methods.

Figure 6 shows the resulting inward radial inward movements for the optimal numerical solutions. The EPB tunneling for Crossrail is associated with small inward movements than decrease monotonically from the crown around to the invert. In contrast, open-face construction of the WB JLE tunnel produces a small outward deformation below the springline.

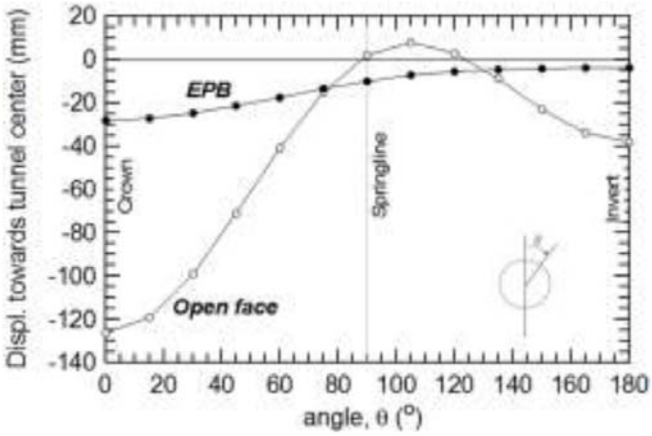

Figure 6. Comparison of the tunnel cavity radial inward movements at the two sites examined

5 CONCLUSIONS

This paper evaluates the sources of ground movements caused by tunneling in stiff overconsolidated London Clay by estimating the deformations occurring at the tunnel cavity (Fig. 1b). The paper compares results using analytical solutions, where the soil mass is characterized as a linearly-elastic half-space, with results from 2D finite element analyses using a relatively advanced soil model (MIT-S1) to represent non-linear stress-strain properties of the clay. In both sets of analyses the cavity deformation mode parameters are back-fitted to the measured data at Greenfield tunnel sections which include measurements of subsurface ground deformations. While the numerical solutions provide a more credible representation of deformations close to the tunnel cavity, the two methods of analyses give broadly similar solutions for far field deformations.

Recent EPB construction of Crossrail tunnels beneath Hyde Park generated much smaller volume loss and lower distortion ratios r at the tunnel cavity than prior open-face construction of the JLE tunnel beneath St James Park. The results confirm that the analytical solutions provide very good approximations for interpreting the distribution of ground movements caused by different methods of tunnel construction, while the numerical solutions provide a more reliable basis for evaluating 3D finite element models of tunnel construction processes

ACKNOWLEDGEMENT

The authors are grateful to the engineers from the BAM-Ferrovial-Kier Joint Venture who provided tremendous help in gathering data from the C300 project. This research was supported by Ferrovial-Agroman through the Ferrovial-MIT program.

REFERENCES

Gasparre, A., Nishimura, S., Minh, N.A., Coop, M.R. and Jardine, R.J. 2007. The stiffness of natural London Clay, *Géotechnique* **57(1)**, 33–47.

GCG 2010. Geotechnical Sectional Interpretative Report 1&2: Royal Oak to Liverpool Street, Volumes 1 and 2 Report" (No. 1D0101-G0G00-00549 and No. 1D0101-G0G00-00550).

Ieronymaki, E.S. (2014) Ph.D in progress, MIT, Cambridge, MA.

Ieronymaki, E.S., Whittle, A.J. and Simic, D. 2014. Ground movements in Hyde Park caused by the Crossrail tunnel construction, *submitted for publication.*

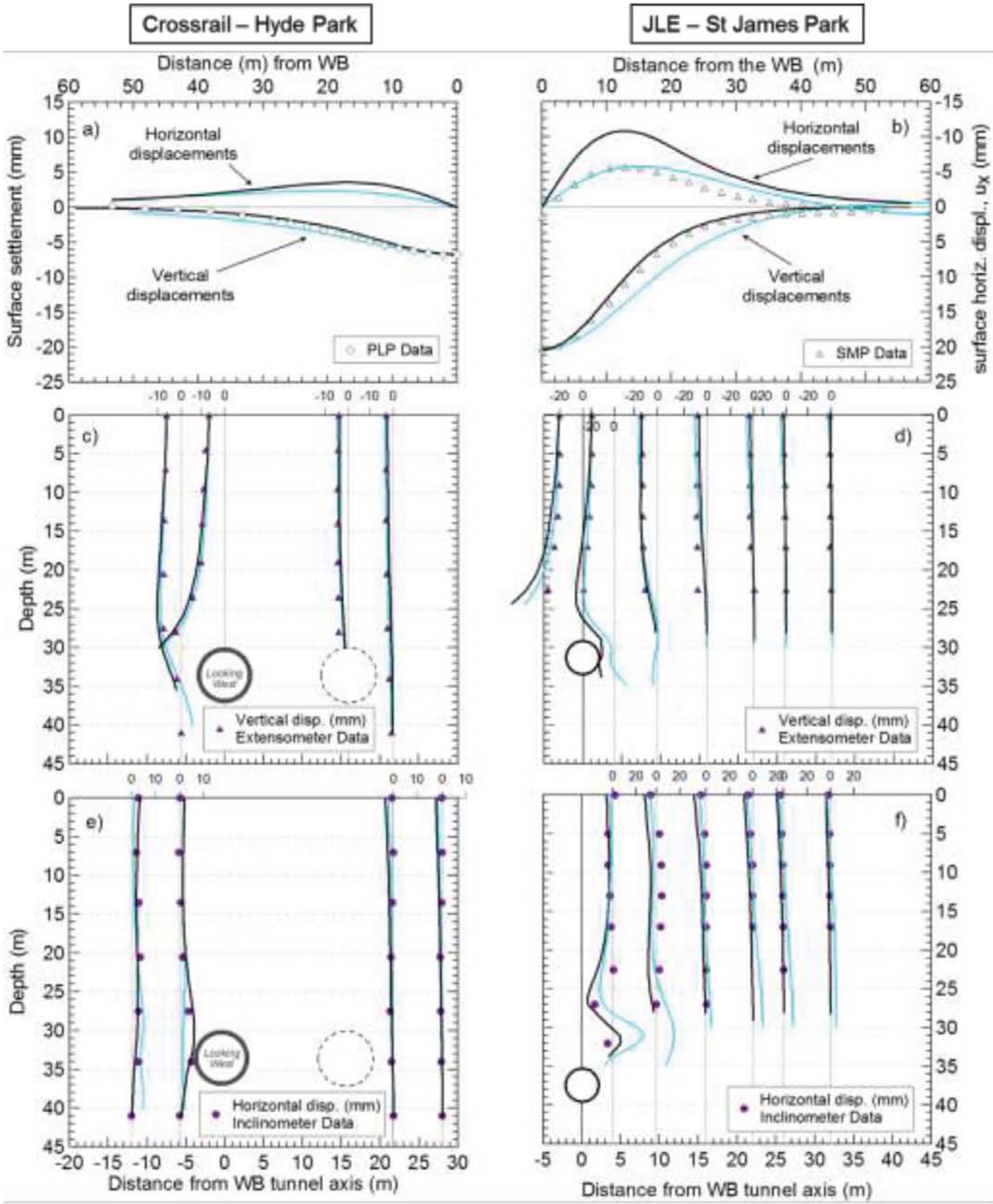

		Crossrail – Hyde Park				JLE – St James Park			
Symbol	Method	$\Delta V_L/V_0$ (%)	u_ε (mm)	ρ	Δu_y (mm)	$\Delta V_L/V_0$ (%)	u_ε (mm)	ρ	Δu_y (mm)
	Analytical	1.00	-18	0.39	-2.6	2.97	-36	1.32	-6.5
	Numerical	0.73	-13	0.23	-12	3.30	-40	1.05	-44

Figure 5. Comparison of optimal analytical and numerical solutions with surface and subsurface ground deformation data for WB Crossrail tunnel below Hyde Park and JLE tunnel below St James Park

Mair, R.J., Taylor, R.N., & Bracegirdle, A. 1993. Subsurface settlement profiles above tunnels in clays. *Géotechnique*, **43(2)**, 315-320

Nyren, R. J. 1998. Field measurements above twin tunnels in London Clay, *PhD thesis*, Imperial College, University of London.

Peck, R.B. 1969. Deep Excavations and Tunnels in Soft Ground. *Active Geotechnics: Proceedings, 7th International Conference on Soil Mechanics and Foundation Engineering* (State of the art Volume), 225-290.

Pestana, J.M. & Whittle A.J. 1999. Formulation of a unified constitutive model for clays and sands, *International Journal for Numerical and Analytical Methods in Geomechanics* **23**, 1215-1243.

Pinto, F., & Whittle, A.J. 2014. Ground Movements due to Shallow Tunnels in Soft Ground. I: Analytical Solutions, *ASCE Journal of Geotechnical and Geoenvironmental Engineering*, **140(4)**, 04013040.

Pinto, F., Zymnis, D., and Whittle, A.J. 2014. Ground Movements due to Shallow Tunnels in Soft Ground. II: Analytical Interpretation and Prediction, *ASCE Journal of Geotechnical and Geoenvironmental Engineering*, **140(4)**, 04013041.

Sagaseta, C. & Whittle, A.J. 2003. Analyzing the effects of gaining and losing ground, *Soil Behavior and Soft Ground Construction,* ASCE GSP No. 119, 255-291.

Standing, J.R. and Burland, J.B. 2006. Unexpected tunnelling volume losses in the Westminster area, London, *Géotechnique,* **56**(1), 11-26.

Verruijt, A. & Booker, J. R. 1996. Surface settlements due to deformation of a tunnel in an elastic half-plane, *Géotechnique*, **46(4)**, 753-756

Zymnis, D.M., Whittle, A.J., & Chatzigiannelis, I. 2013. Effect of anisotropy on ground movements caused by tunneling, *Géotechnique,* **63(13)**, 1083-1102.

Analytical strain estimation of curved buried pipelines due to permanent ground displacements

Estimation analitique des tensions dans les conduites courbes enterrées en cas de déplacements permanents du sol

D.K. Karamitros, G.D. Bouckovalas and C. Zoupantis

ABSTRACT Existing analytical methodologies for the strength verification of buried steel pipelines against large permanent ground displacements (PGDs), such as active fault ruptures, apply only to straight pipelines, not taking into account bends existing in their route. To fill this gap in the relevant literature, a new methodology is proposed herein, for the analytical computation of pipeline strains developing in the presence of bends with arbitrary geometry (bend angle and radius of curvature), located outside the PGD high-curvature zone, but within the pipeline's unanchored length. Comparison with results from 3D non-linear finite element analyses indicates that the proposed methodology captures the basic mechanisms of pipeline response, with both quantitative and qualitative accuracy. Additional conclusions of practical interest for pipeline design are finally drawn from a joint review of the numerical and analytical predictions.

1 INTRODUCTION

Permanent ground displacements (PGDs) is probably one of the most critical loading conditions that need to be taken into account for the design of buried pipelines (e.g. ALA-ASCE, 2004, O'Rourke & Liu, 1999). In earthquake-prone areas, such displacements are mainly associated to the rupture of active faults, although they may also originate from more common geotechnical causes, such as slope failures, underground works, differential heave or settlement, lateral spreading, etc. In either case, a rigorous computation of pipeline strains requires the use of numerical analyses which take consistently into account the 3D geometry of the pipeline axis, the non-linear response of the pipeline steel and the surrounding backfill material, as well as large-displacement-induced second order effects (e.g. Xie et al, 2011, Vazouras et al, 2012). Nevertheless, these numerical analyses require considerable expertise and they are time consuming, thus engineers are increasingly relying upon user friendly analytical solutions, which allow parametric analyses to be performed at a fraction of the time required for a consistent numerical investigation (e.g. Karamitros et al, 2007, 2011, Trifonov & Cherniy, 2010, 2012).

A common simplification of the analytical solutions is that the pipeline axis is considered straight for a large distance from the applied PGD. The only (known to the Authors) exception is the analytical solution proposed by O'Rourke & Liu (1999), which takes into account the existence of bends in the vicinity of the PGD. Nevertheless, the range of application of this solution is limited by a number of simplifying assumptions, namely that it refers exclusively to 90° bends, it does not take into account the arch-shaped geometry of the bend, while the pipeline steel is assumed to behave elastically.

To this extent, the present study attempts to remedy the above limitations. More specifically, based on the elastic beam theory, an analytical solution is presented for the verification of pipelines with curved bends, for a wide range of bend angles, curvature radii, bend to PGD-zone distances, as well as tensile displacements applied to the pipeline. A bilinear stress-strain relationship is considered for the pipeline steel, through an iterative equivalent linear solution scheme, while the Winkler-type soil springs are taken as elastic-perfectly plastic. Following an analytical presentation of the basic modelling assumptions and the resulting equations, the accuracy of the analytical predictions is evaluated against the results of 3D numerical analyses with the Finite Element Method.

2 PROPOSED ANALYTICAL METHODOLOGY

2.1 Basic Assumptions

The proposed methodology initially focuses upon the calculation of axial and bending strains in the zone of the pipeline bend, which is considered to lie away from the high-curvature zone, near the applied PGD, but within the pipeline's unanchored length (Step 1). This part of the pipeline is analysed using the direct stiffness method, as an arched elastic beam with an equivalent secant Young's modulus, in order to indirectly take into account the non-linear behaviour of pipeline steel.

The pipeline's behaviour near the bend is derived as a function of the axial component of the applied PGD, by employing equations of displacement compatibility (Step 2). This procedure allows the calculation of the axial force developed in the pipeline at the applied PGD zone. This force can be used in any of the existing analytical methodologies for the strength verification of pipelines near fault crossings, allowing the quantification of the effect of the pipeline's geometry on the strains developing within the PGD zone (Step 3).

2.2 Step 1: Analysis of the bend

The bent part of the pipeline is analysed as an arched elastic beam, with an axial displacement u_A being applied at its end A, as shown in Figure 1. A rotational and a transverse transitional spring are considered to support the beam at point A, while an axial and a transverse spring are considered at point B. The spring constants are computed in the following paragraphs. It should be noted that preliminary numerical analyses, such as the ones presented in the following Section, indicated that the bending moment developing at point B is very small, thus no rotational spring was considered at that end of the beam. Apart from the aforementioned supports, the beam is loaded with an axial uniformly distributed load t_u equal to the ultimate friction force applied by the surrounding soil, as well as a transverse load q_u, equal to the ultimate soil resistance for transverse pipeline displacement.

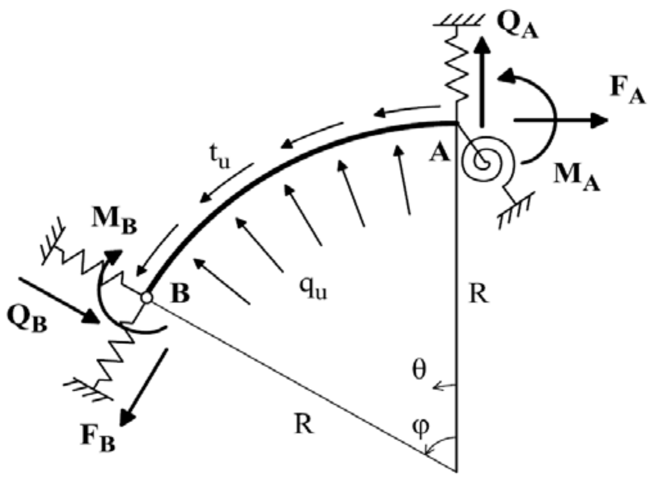

Figure 1. Model of the arched pipeline bend.

The beam is solved using the direct stiffness method:

$$\{P\}-\{P_L\}=\left(\left[K\right]+\left[K_{spr}\right]\right)\{u\} \tag{1}$$

where $\{P\}=\{F_A\ Q_A\ M_A\ F_B\ Q_B\ M_B\}T$ are the developing axial forces F, shear forces Q and bending moments M at the ends A and B of the beam, $\{P_L\}$ are the respective reaction forces corresponding to loads t_u and q_u, [K] is the stiffness matrix of the arched beam, $[K_{spr}]$ is the springs matrix and $\{u\}=\{u_A\ v_A\ \varphi_A\ u_B\ v_B\ \varphi_B\}T$ are the axial displacements u, the transverse displacements v and the rotations φ of the ends A and B of the beam.

Considering the beam's equilibrium without the external loads t_u and q_u, yields:

$$\{P_B\}=\begin{Bmatrix}F_B\\Q_B\\M_B\end{Bmatrix}=\begin{bmatrix}\cos\varphi & \sin\varphi & 0\\ -\sin\varphi & \cos\varphi & 0\\ R(\cos\varphi-1) & R\sin\varphi & 1\end{bmatrix}\begin{Bmatrix}F_A\\Q_A\\M_A\end{Bmatrix}$$
$$\Rightarrow\{P_B\}=[\Lambda]\{P_A\} \tag{2}$$

Therefore, the stiffness matrix [K] can be calculated with the aid of the above transpose matrix [Λ]:

$$[K]=\begin{bmatrix}[F]^{-1} & \left([F]^{-1}\right)^T[\Lambda]^T\\ [\Lambda][F]^{-1} & [\Lambda]\left([F]^{-1}\right)^T[\Lambda]^T\end{bmatrix} \tag{3}$$

where [F] is the flexibility matrix of an arched beam, similar to the one examined herein, but with a fixed support at point B and with no supports at point A. The elements of this flexibility matrix can be calculated using the principle of virtual work:

$$[F]=\begin{bmatrix}\frac{R^3}{EI}\left(\frac{3\varphi}{2}+\frac{\sin2\varphi}{4}-2\sin\varphi\right) & \frac{R^3}{EI}\left(\cos\varphi-\frac{\cos2\varphi}{4}-\frac{3}{4}\right) & \frac{R^2}{EI}(\sin\varphi-\varphi)\\ & \frac{R^3}{EI}\left(\frac{\varphi}{2}-\frac{\sin2\varphi}{4}\right) & \frac{R^2}{EI}(1-\cos\varphi)\\ & & \frac{R}{EI}\varphi\end{bmatrix} \tag{4}$$

Considering the same arched cantilever beam, with a fixed support at point B, the reactions to the applied soil friction forces t_u and the transverse soil resistance forces q_u may be calculated using equations of equilibrium:

$$\{P_{BL}\}=\begin{Bmatrix}F_{BL}\\Q_{BL}\\M_{BL}\end{Bmatrix}=\begin{Bmatrix}Rq_u(1-\cos\varphi)-Rt_u\sin\varphi\\ Rq_u\sin\varphi+Rt_u(1-\cos\varphi)\\ R^2t_u(\varphi-\sin\varphi)+R^2q_u(1-\cos\varphi)\end{Bmatrix} \tag{5}$$

The corresponding axial displacement (i=1), transverse displacement (i=2) and rotation (i=3) of point A may be calculated with the aid of the principle of virtual works:

$$\{\Delta_{AL}\}=\frac{R^3}{EI}\cdot\begin{Bmatrix}t_uR\left(\varphi\sin\varphi-\frac{\varphi^2}{2}-\frac{\sin^2\varphi}{2}\right)\\ +q_uR\left(2\sin\varphi-\frac{\sin2\varphi}{4}-\frac{3\varphi}{2}\right)\\ t_uR\left(\sin\varphi-\varphi\cos\varphi-\frac{\varphi}{2}+\frac{\sin2\varphi}{4}\right)\\ +q_uR\left(1-\cos\varphi-\frac{\sin^2\varphi}{2}\right)\\ t_u\left(\frac{\varphi^2}{2}+\cos\varphi-1\right)\\ +q_u(\varphi-\sin\varphi)\end{Bmatrix} \tag{6}$$

Utilizing the above matrix, in combination with [F] and [Λ], the reaction matrix $\{P_L\}$ may be formed:

$$\{P_L\}=\begin{Bmatrix}[F]^{-1}\{\Delta_{AL}\}\\ [\Lambda][F]^{-1}\{\Delta_{AL}\}+\{P_{BL}\}\end{Bmatrix} \tag{7}$$

The opposite of this matrix is applied to the beam as a loading, as indicated by Equation 1.

The constants of the transverse and rotational springs that have been considered to support the ends A and B of the examined arched beam are calculated assuming that the pipeline away from the bend is behaving as a semi-infinite elastic beam on elastic foundation, with a Winkler-type spring constant equal to k. Therefore, the elastic line w away from A and B may be described as:

$$w=e^{-\lambda x}C_1\sin\lambda x+e^{-\lambda x}C_2\cos\lambda x \tag{8a}$$
$$\text{where: } \lambda=\sqrt[4]{\frac{k}{4E_1I}} \tag{8b}$$

Taking also into account that M=-EIw'' and Q=EIw''', the following boundary conditions may be derived:

$$Q(0)=4EI\lambda^3w(0)+2EI\lambda^2w'(0) \tag{9}$$
$$M(0)=2EI\lambda w'(0)+2EI\lambda^2w(0) \tag{10}$$

Equations 9 and 10 essentially provide the spring constants for the supports of node A. For node B, there is no rotational spring, thus M(0)=0. Therefore:

$$Q(0)=2EI\lambda^3w(0) \tag{11}$$

It should be noted that Equations 9 and 10 are coupled, thus the spring matrix contains non-zero elements outside the main diagonal.

As far as the axial spring at end B of the arched beam is concerned, its constant may be calculated by examining the axial stress and strain distribution in the straight part of the pipeline, away from the bend. More specifically, the axial force developing in this part of the pipeline is linearly decreasing with the distance from point B, due to the constant friction force t_u applied by the surrounding soil, until it becomes zero at a distance $L_{anch}=F_B/t_u$. The elongation of this part of the pipeline can be calculated by considering elastic behaviour for the pipeline steel and integrating the strains along its length:

$$u_B=\int_0^{L_{anch}}\varepsilon(x)dx=\int_0^{L_{anch}}\frac{F_B-t_ux}{E_1A}dx=\frac{F_B{}^2}{2E_1At_u} \tag{12}$$

The constant for the axial spring at node B may be therefore calculated as follows:

$$k_{u,B}=\frac{dF_B}{du_B}=\frac{E_1At_u}{F_B} \tag{13}$$

It should be observed that the above constant is a function of the axial force at point B, which is not a priori known. Therefore, the analysis of the pipeline needs to be performed iteratively, until convergence is achieved.

According to the above, the spring matrix is constructed as follows:

$$[K_{springs}]=\begin{bmatrix}0&0&0&0&0&0\\0&4EI\lambda^3&2EI\lambda^2&0&0&0\\0&2EI\lambda^2&2EI\lambda&0&0&0\\0&0&0&EAt_u/F_B&0&0\\0&0&0&0&2EI\lambda^3&0\\0&0&0&0&0&0\end{bmatrix}\qquad(14)$$

Finally, the following system of equations is derived:

$$\begin{Bmatrix}\{P_s\}_{1x1}\\\{P_f\}_{5x1}\end{Bmatrix}=\begin{bmatrix}[K_{ss}]_{1x1}&[K_{sf}]_{1x5}\\[K_{fs}]_{5x1}&[K_{ff}]_{5x5}\end{bmatrix}\begin{Bmatrix}\{u_s\}_{1x1}\\\{u_f\}_{5x1}\end{Bmatrix}\qquad(15)$$

The unknown quantities in Equation 15 are the axial force at node A $\{P_s\}=F_A$ and the displacements $\{u_f\}=\{v_A\ \varphi_A\ u_B\ v_B\ \varphi_B\}T$, which are calculated according to the applied displacement $\{u_s\}=u_A$, as:

$$\{u_f\}=[K_{ff}]^{-1}(\{P_f\}-[K_{fs}]\{u_s\})\qquad(16)$$

$$\{P_s\}=[K_{ss}]\{u_s\}+[K_{sf}]\{u_f\}\qquad(17)$$

The distribution of bending moments and axial forces can be consequently derived as:

$$M=M_A+Q_A R\sin\theta-F_A(R-R\cos\theta)$$
$$+R^2t_u(\varphi-\sin\theta)-R^2q_u(\cos\theta-1)\qquad(18)$$

$$F=F_A\cos\theta+Q_A\sin\theta$$
$$-Rq_u(\cos\theta-1)-Rt_u\sin\theta\qquad(19)$$

In the previously presented solution, the pipeline was considered to behave elastically. In order to account for the non-linear behaviour of the pipeline steel, the above procedure is repeated, using an equivalent secant Young's modulus E΄ for the pipeline steel, in order to achieve compatibility between the stresses and strains developing on the pipeline, at the position where the maximum bending moment M_{max} occurs. The procedure adopted for this purpose is the same one proposed by Karamitros et al (2007, 2011), which is also employed by Trifonov & Cherniy (2010, 2012). According to this procedure, the exact distribution of stresses and strains on the pipeline's cross-section is computed, as a function of the maximum developing axial fore and bending moment, considering a bilinear stress-strain relationship for the pipeline steel. An equivalent secant Young's modulus is consequently estimated, from the relationship between the bending moments and the bending strains, and the above procedure (i.e. Step 1) is then repeated, until convergence is accomplished.

2.3 Step 2: Pipeline bend – PGD zone interaction

The interaction between the curved part of the pipeline and the applied PGD is quantified by considering the compatibility between the developing axial strains along the pipeline, the pipeline's elongation due to the axial component Δx of the applied PGD, as well as the displacement u_A of point A, at the bend. The distribution of axial strains is determined by considering an elastic stress-strain behavior for the pipeline steel, as well as a linear distribution of axial forces along the pipeline, due to the constant value of the friction force t_u applied by the surrounding soil. More specifically, in the side of the bend, the axial force varies from F_A at point A of the bend, to $F_{fault}=F_A+t_uL_A$ at the PGD location, while, in the other side, the axial force varies from F_{fault} at the PGD location, to F=0, at a distance $L_{anch}=F_{fault}/t_u$, as shown in Figure 2. According to the above:

$$\Delta x=u_A+\int_0^{L_A}\frac{F_A+t_u x}{EA}dx+\int_0^{L_{anch}}\frac{F_{fault}-t_u x}{EA}dx\Rightarrow$$
$$u_A=\Delta x-\frac{2F_AL_A+t_uL_A^2+{F_A^2}/{2t_u}}{EA}\qquad(20)$$

The axial force F_A in Equation 20 is not a priori known. Therefore, a value of FA=0 is initially considered, allowing for the estimation of an initial displacement u_A, which is subsequently applied to node A of the pipeline bend. The axial force F_A is then calculated from the first step of the methodology, the displacement u_A is consequently redefined using Equation 20 and the procedure is repeated until convergence is accomplished.

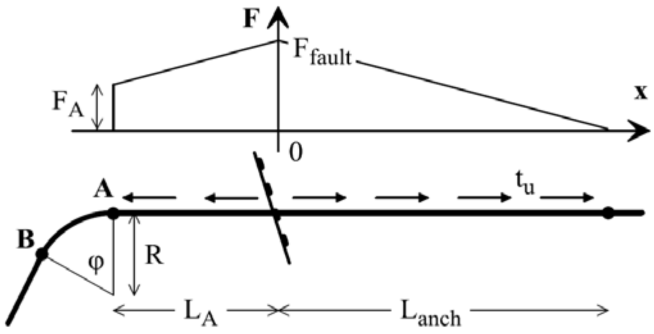

Figure 2. Pipeline axial force distribution.

2.4 Step 3: Strength verification in the PGD zone

Having calculated the axial force F_A at point A of the pipeline's bend, the axial force F_{fault} at the PGD zone may also be calculated as described in Step 2. This force can be subsequently implemented into any of the existing methodologies for the strength verification of straight pipelines at fault crossings (e.g. Karamitros et al, 2007, Karamitros et al, 2012, Trivonov & Cherniy, 2011), allowing the quantification of the effect of the bend, on the strains developing in the PGD high-curvature zone.

3 EVALUATION OF PROPOSED METHODOLOGY

The accuracy of the proposed methodology was evaluated through comparison with numerical predictions from parametric numerical analyses with the Finite Element code ANSYS 12. In more detail, numerical analyses were performed for a 0.9144m (36'') diameter high pressure natural gas pipeline, with 0.0119m wall thickness, made of API5L-X65 carbon steel. The pipeline was discretized into 0.50m long elastoplastic beam elements, while the interaction with the backfill was simulated with elastoplastic Winkler-type springs, defined according to ALAASCE (2005) guidelines for 1.30m thick cover of silica sand with friction angle φ=36º and dry unit weight γ=18KN/m2. The pipeline route included a bend of angle φ, which varied parametrically from 0° (straight axis) to 90°, with a radius of curvature R, which similarly varied between 5D and 40D, where D is the nominal pipe diameter. The pipeline axis crossed the trace of a strike-slip fault at a crossing angle of 45° and a distance LA from the bend, which varied parametrically from 50D to 200D. Permanent ground displacements of up to 2.0D were applied at the fixed end of the Winkler springs which overlay the sliding wall of the fault. Note that the parametric analyses were performed with reference to a basic case with L_A/D=100, φ=45° and R/D=10.

The results from the numerical analyses are compared against the analytical predictions in Figure 3, in terms of maximum pipeline strains developing at the bend, as well as in the vicinity of the fault crossing. The agreement in all graphs is fairly consistent, indicating that the proposed methodology captures the basic mechanisms of pipeline response with both quantitative and qualitative accuracy, thus it may be readily used for preliminary design purposes.

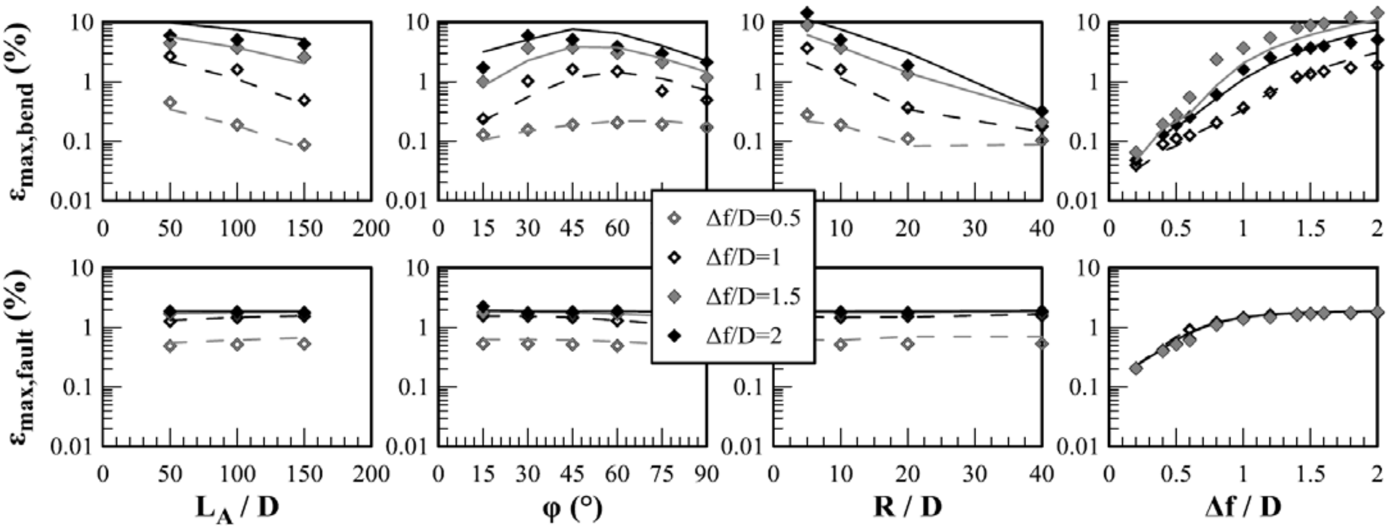

Figure 3. Comparison between numerical results (points) and analytical predictions (lines).

4 CONCLUDING REMARKS

The numerical and analytical predictions reviewed in this study (i.e. Figure 3) reveal a number of conclusions of practical interest for the pipeline design, namely that:

- The effect of bends on pipeline strains at the zone of the applied PGD is relatively minor. Hence, pipeline strains in this region may be computed with methods developed for straight pipelines.
- As the applied displacements increase and/or the distance of bends from the PGD decreases, pipeline strains at the bend gradually exceed the strains at the PGD zone, and become critical for the pipeline design. The difference may reach an order of magnitude, for bend angles between 30-45° and small radii of curvature (R/D=5÷10).
- The most severe bend angle is not 90°, but ranges between 30° and 45°.
- The accurate modelling of the curved geometry of the pipeline plays an important role in both for analytical and numerical simulations, as the developing pipeline strains are very sensitive on the bend's radius of curvature.
- Increasing the radius of curvature is an efficient way to reduce pipeline strains at the bends.

Finally, note that the present study is still in progress, aiming to further refine the analytical predictions for large applied displacements, small distances from the applied PGD and small radii of curvature, as well as, to come up with more solid guidelines and design recommendations.

REFERENCES

American Lifelines Alliance - ASCE (2005): "Guidelines for the Design of Buried Steel Pipe", July 2001 (with addenda through February 2005).

Karamitros, D.K., Bouckovalas, G.D., Kouretzis, G.P. 2007. Stress analysis of buried steel pipelines at strike-slip fault crossings, *Soil Dynamics and Earthquake Engineering* **27 (3)**, 200-211.

Karamitros, D.K., Bouckovalas, G.D., Kouretzis, G.P., Gkesouli, V. 2011. An analytical method for strength verification of buried steel pipelines at normal fault crossings, *Soil Dynamics and Earthquake Engineering* **31 (11)**, 1452-1464.

O'Rourke M.J, Liu X. 1999. *Response of buried pipelines subject to earthquake effects*, Monograph Series, Multidisciplinary Center for Earthquake Engineering Research (MCEER).

Trifonov, O.V., Cherniy, V.P. 2010. A semi-analytical approach to a nonlinear stress-strain analysis of buried steel pipelines crossing active faults, *Soil Dynamics and Earthquake Engineering* **30 (11)**, 1298-1308.

Trifonov, O.V., Cherniy, V.P. 2012. Elastoplastic stress-strain analysis of buried steel pipelines subjected to fault displacements with account for service loads, *Soil Dynamics and Earthquake Engineering* **33 (1)**, 54-62.

Vazouras, P., Karamanos, S.A., Dakoulas, P. 2012. Mechanical behavior of buried steel pipes crossing active strike-slip faults, *Soil Dynamics and Earthquake Engineering* **41**, 164-180.

Xie X., Symans M. D., O'Rourke M. J., Abdoun T. H., O' Rourke T. D., Palmer M. C. & Stewart H. E. 2011. Numerical modeling of buried HDPE Pipelines subjected to strike-slip faulting, *Journal of Earthquake Engineering* **15**, 1273–1296.

Implementation of a viscoplastic Mohr-Coulomb material model for the simulation of time effects in tunnel excavations

La mise en oeuvre d'un modèle viscoplastique de matériau Mohr-Coulomb pour la simulation des effets du temps dans les fouilles de tunnels

F.E. Karaoulanis, T.N. Chatzigogos

ABSTRACT The implementation of a viscoplastic model based on the well known Mohr-Coulomb criterion, is presented this work. Post yield behavior is assumed to be characterized by perfect plasticity while the rate-dependent behavior is modeled by a suitable generalization of the Duvaut-Lions viscoplastic model. The proposed model is then implemented in a finite element code and applied to a typical tunnel excavation problem. The time evolution of the radial displacements for an unsupported part of the tunnel during construction is evaluated and used as a case study. Furthermore the influence of the viscosity parameter η in the overall structure response is examined through a series of parametric studies.

1 INTRODUCTION

Time dependent effects such as creep and relaxation are often exhibited during tunnel excavations (Cristescu & Hunsche, 1998). In order to realistically describe these effects, several models are proposed in the literature, most of which fall into three main categories: empirical models, viscoelastic models and viscoplastic models, with the last ones to be considered here. Assuming small strains and strain rate depended models, viscoplasticity requires a yield surface to describe the elastic domain and a timedependent formulation for the definition of the plastic strain rate. Typically the former is provided by a suitable material model like the Mohr-Coulomb, while for the latter the Perzyna formulation is commonly employed (see e.g. Reed, 1988). However, within the context of the Finite Element Method and the stress update algorithm, the Mohr-Coulomb yield criterion is well known for the severe algorithmic and numerical complexities that it introduces due to the singularities induced by the nonsmooth intersections of the yield surfaces that describe it. Furthermore, the Perzyna formulation can be proven not to be applicable in nonsmooth multisurface plasticity, leading to unrealistic results when used (Simo & Hughes, 1998).

In this article, a numerical implementation of the Mohr-Coulomb yield criterion is presented, based on the spectral representation of the stress tensor. It is shown, that the complexities introduced by the nonsmooth yield surface eliminate and a general, simple and extremely robust algorithm is obtained. The extension to viscoplasticity is accomplished by employing the Duvaut-Lions formulation. A numerical example regarding the simulation of time effects in tunnel excavations is provided, to demonstrate the proposed approach.

2 STATE OF ART

Several authors have employed elastic-viscoplastic models to predict the stress-strain-time behavior of geomaterials either excluding (Reed, 1988) or including some form of hardening (Cristescu 1987; Desai & Zhang, 1987; Datcheva *et al* 2001). The yield criteria and the corresponding plastic potentials used involve either single (Desai & Zhang, 1987) or multiple surfaces (Reed, 1988; Cristescu 1987; Datcheva *et al* 2001). However, all the above mentioned approaches follow the Perzyna formulation, which it can be proven not always to reduce to the rate independent solution (Simo & Hughes, 1998).

Furthermore, singularities rising due to the nonsmoothness of the Mohr-Coulomb yield surface introduce severe complexities that lead to different numerical approaches, proposed algorithms and computer implementations. Hence, from a computational standpoint, effort has been initially directed towards replacing the yield surface in near singular areas (see e.g. Owen's & Hinton's (1980) work, where the authors proposed the replacement of Mohr-Coulomb and Tresca surfaces by Drucker-Prager's and Von-Mises' ones respectively, leading inevitably to a gradient jump) or smoothing the yield surface in these areas (e.g. by modifying the yield surface in the vicinity of singularities as by Sloan & Booker (1986)). In early 1990s and within the context of the return mapping algorithm (Simo & Hughes, 1998), efforts have been focused on the proper implementation of the plastic corrector in near corner regions following specific surface dependent approaches.

The extension of classical plasticity models to accommodate non-smooth yield surfaces goes back to the fundamental work of Koiter (1960). Later formulations of plasticity employing convex analysis as in Moreau (1976) encompass these classical treatments as a particular case. Recent formulations are usually based on the work of Simo & Hughes (1998) where the standard Kuhn-Tucker complementarity conditions are used to provide the characterization of plastic loading/unloading.

In this work, the above treatment is reformulated and implemented using the spectral decomposition of the stress tensor. It is then applied to the elastic-perfectly plastic Mohr-Coulomb yield criterion and finally is extended to accommodate the rate dependent behavior, following the Duvaut-Lions approach (Duvaut & Lions, 1976). All the complexities introduced by the non-smooth yield surface eliminate and a general, simple and extremely robust algorithm is obtained, capable of modeling time dependent behavior. The theoretical framework of the proposed methodology is described in depth in previous works by the authors (Karaoulanis 2010; 2013; Karaoulanis & Chatzigogos 2010) along with implementation details for different material models (Karaoulanis 2008; 2009; 2011).

3 NUMERICAL IMPLEMENTATION

3.1 Governing equations

Let $\boldsymbol{\varepsilon}\in\Re$ denote the total strain tensor at a fixed point of a solid $\mathbf{X}\in\Re^{ndim}$, where $n_{\dim}\in\{1,2,3\}$. In the infinitesimal case, the strains $\boldsymbol{\varepsilon}$ are simply identified as the symmetric part of the gradient of the displacement vector and are assumed additively decomposed, as:

$$\boldsymbol{\varepsilon} = \boldsymbol{\varepsilon}^e + \boldsymbol{\varepsilon}^p \tag{1}$$

where $\boldsymbol{\varepsilon}^e$ and $\boldsymbol{\varepsilon}^p$ refers to the elastic and plastic strain parts respectively. Assuming a hyperelastic material, $\boldsymbol{\varepsilon}^e$ is related to the stress tensor through a stored energy function,

$$\boldsymbol{\sigma} = \frac{\partial W}{\partial \boldsymbol{\varepsilon}^e} = \boldsymbol{C}\boldsymbol{\varepsilon}^e \tag{2}$$

where $\boldsymbol{C}$ is the well known elasticity matrix. The plastic part is given from the flow rule, which according to Koiter (1960) reads for the multisurface plasticity:

$$\dot{\boldsymbol{\varepsilon}}^p = \sum_{a=1}^{n} \dot{\lambda}^a \frac{\partial g_\alpha(\boldsymbol{\sigma})}{\partial \boldsymbol{\sigma}} \tag{3}$$

Functions $g_a(\boldsymbol{\sigma}):\Re^{n\sigma}\to\Re$, $a\geq1$, define a plastic potential, which dictates the direction of the plastic flow. The parameters λ^a are nonnegative scalars, called the consistency parameters, which are assumed to obey the following Karush–Kuhn–Tucker coplementarity conditions and the consistency requirement:

$$\dot{\lambda}^a \geq 0,\ f_\alpha \leq 0,\ \dot{\lambda}^a f_\alpha = 0,\ \lambda^a \dot{f}_\alpha = 0 \qquad (4)$$

Finally the functions with $f_\alpha(\boldsymbol{\sigma}):\Re^{n\sigma}\rightarrow\Re$, $a\geq 1$, are usually known as yield functions, assumed to intersect non-smoothly in what follows and define the so called elastic domain, i.e. the following convex set,

$$\mathrm{E}_\sigma = \{\boldsymbol{\sigma} \in \Re^{n\sigma} : f_\alpha(\boldsymbol{\sigma}) \leq 0,\ \forall a \in [1,2,m]\} \qquad (5)$$

with m being the number of the constraints. Of special importance is the case where $f_\alpha \equiv g_\alpha$, which goes by the name associative flow rule.

3.2 Spectral decomposition

Now recall that according to the Spectral Theorem, the spectral decomposition of the stress tensor is given as:

$$\boldsymbol{\sigma}_{n+1} = \boldsymbol{\sigma}_{\mathrm{A}(n+1)} \boldsymbol{m}^A, \quad \boldsymbol{m}^A = \boldsymbol{n}^{(A)} \otimes \boldsymbol{n}^{(A)} \qquad (6)$$

where $\boldsymbol{\sigma}_{\mathrm{A}}$ and $\boldsymbol{n}_{\mathrm{A}}$ are the principal Cauchy stresses and directions respectively, A={1,2,3} and Einstein's summation convention is assumed, except for indices in parentheses. Therefore, gradients of f and g, may be defined as

$$\partial_\sigma f = \frac{\partial f}{\partial \boldsymbol{\sigma}_A} \boldsymbol{m}^A, \partial_\sigma g = \frac{\partial g}{\partial \boldsymbol{\sigma}_A} \boldsymbol{m}^A. \qquad (7)$$

3.3 Numerical integration

If isotropy in the elastic response is assumed, then it can be easily shown that the strain spectral directions coincide with the stress spectral directions and therefore a solution algorithm can be formulated in the principal stress space. Employing a backward Euler integration procedure and a Newton-Raphson integration scheme the following residual vector, Jacobian matrix and vector of unknowns yield:

$$r^{(k)} = \begin{bmatrix} \varepsilon^e_A - \varepsilon^{e,trial}_A + \sum_{a=1}^{m_{act}} \Delta\lambda^a \partial_{\boldsymbol{\sigma}_A} g_a \\ f_a \end{bmatrix}_{n+1}^{(k)} \qquad (8)$$

$$J^{(k)} = \begin{bmatrix} \mathbf{c}^{-1} + \sum_{a=1}^{m_{act}} \Delta\lambda^a \partial_{\boldsymbol{\sigma}_A \boldsymbol{\sigma}_A} g_a & \partial_{\boldsymbol{\sigma}_A} g_a \\ \partial_{\boldsymbol{\sigma}_A} f_a & 0 \end{bmatrix}_{n+1}^{(k)} \qquad (9)$$

$$x^{(k)} = \begin{bmatrix} \delta\boldsymbol{\sigma}_A \\ \delta\lambda^a \end{bmatrix}^{(k)} \quad x^{(0)} = \begin{bmatrix} \boldsymbol{\sigma}^{trial}_{A,n+1} \\ 0 \end{bmatrix}^{(k)} \quad k \leftarrow k+1 \qquad (10)$$

The stress tensor and the consistency parameters are updated incrementally, as:

$$\boldsymbol{\sigma}^{(k)}_{cor} = \boldsymbol{\sigma}_{trial} + \sum \delta\boldsymbol{\sigma}^{(k)}, \quad \Delta\lambda^\alpha = \sum_k \delta\lambda^{\alpha(k)} \qquad (11)$$

Finally, the active set of the yield functions, defined as $\boldsymbol{J}_{act}$ = {α∈{1,2,...,m}| $f^{trial}_{a,n+1}$ > 0} is considered constant during the entire iteration process. When all constraints $f_{\alpha,n+1} = 0$ are eventually satisfied for every α, the local Newton iteration scheme is exited and the solution is further checked against non negative Δλ. If the latter is not satisfied for some constraint, then the corresponding yield surface is marked as inactive and dropped from the updated set of the active constraints.

3.4 Viscoplasticity

It can be easily proven that the Perzyna viscoplastic formulation is not suitable for multisurface plasticity, since it does not always reduce to the rate independent case (Simo & Hughes, 1998). Therefore a viscoplasticity formulation, closely related to a model originally developed by Duvaut & Lions (1976) is utilized, which in first order accuracy gives for the stresses:

$$\boldsymbol{\sigma}_{n+1} = \frac{\boldsymbol{\sigma}^{trial}_{n+1} + (\Delta t/\eta)\bar{\boldsymbol{\sigma}}_{n+1}}{1 + \Delta t/\eta} \qquad (12)$$

where η is a fluidity like parameter, Δt the corresponding time step and $\bar{\boldsymbol{\sigma}}_{n+1}$ the time-independent (in viscid) solution. Furthermore, the above formulation can be further extended to include more elaborate models, employing any type of C_1 monotonic functions, typically exponentials and power laws (Simo & Hughes, 1998).

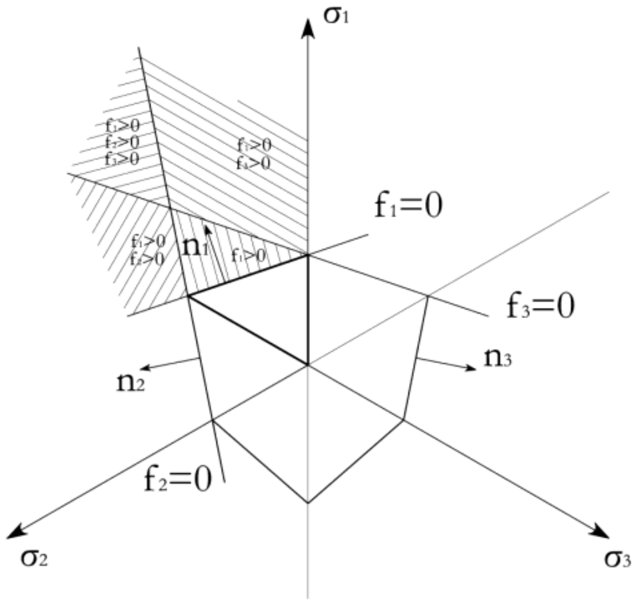

Figure 1. The Mohr-Coulomb criterion in the deviatoric plane.

3.5 Application to the Mohr Coulomb yield criterion

The well known Mohr-Coulomb criterion given in terms of maximum and minimum principal stresses reads:

$$f = (\sigma_{\max} - \sigma_{\min}) + (\sigma_{\max} + \sigma_{\min})\sin(\phi) - 2c\cos(\phi) \qquad (13)$$

where φ is the internal friction angle and c the cohesion. Six equations can be derived from (14), assuming however that $\sigma_1 \geq \sigma_2 \geq \sigma_3$ the number of the yield functions describing the model can be reduced to the following three:

$$f_1 = \sigma_1 - \sigma_3 - \sigma_y,\ f_2 = \sigma_2 - \sigma_3 - \sigma_y \\ f_3 = \sigma_1 - \sigma_2 - \sigma_y \qquad (14)$$

The first derivatives can be easily shown that they are constant while the second ones are zero,

$$\frac{df_1}{d\sigma} = \begin{bmatrix} +1+\sin(\phi) \\ 0 \\ -1+\sin(\phi) \end{bmatrix}, \quad \frac{df_2}{d\sigma} = \begin{bmatrix} 0 \\ +1+\sin(\phi) \\ -1+\sin(\phi) \end{bmatrix}, \quad \frac{df_3}{d\sigma} = \begin{bmatrix} +1+\sin(\phi) \\ -1+\sin(\phi) \\ 0 \end{bmatrix} \tag{15}$$

leading to a linear system of equations. It can be observed that the derivatives are defined everywhere, compared to the case where the yield surfaces are defined using the stress invariants; therefore the robustness and the accuracy of the solution is vastly improved. Furthermore, the derivatives are constant, leading to a closed form type solution, not requiring a local Newton iteration scheme and thus greatly reducing the computational cost.

4 APPLICATION

The proposed model has been implemented in the general purpose finite element program *nemesis* (Karaoulanis, 2014), developed by the first author. In what follows, the application of the above proposed algorithm is presented, in a typical tunnel of circular cross section. The objectives of this case study are:

- To demonstrate the proposed algorithm.
- To propose a methodology on describing the time evolution of the radial displacements for an unsupported part of the tunnel during construction.
- To examine the influence of the viscosity parameter η in the overall structure response.

The finite element model employed consists of 5487 nodes. The soil mass is modeled by 4200 typical displacement based, eight node hexahedral elements. The lining, when applicable, is modeled by MITC4 shell elements. The material properties used are summarized in **Table 1**.

Table 1. Material properties.

Property	Value
Young modulus , E (soil)	100MPa
Poisson ratio, ν (soil)	0.20
Cohesion, c	500KPa
Friction angle, φ	22^0
Dilation angle, ψ	22^0
Young modulus , E (lining)	29GPa
Poisson ratio, ν (lining)	0.3

The simulation domain is considered to be initially under isotropic stress conditions equal to σ_0 = 2MPa. Then, the excavation is modeled in sequential construction steps, where in each step the front is moving by 2.0m and lining is applied. In any case however there exists a part of the tunnel with a length equal to *D*, which remains unsupported. As soon as 15 excavation steps are completed, the excavation procedure is stopped and the analysis is further carried for another 2500 steps, each assumed a duration Δt=1 (note that time units are canceled out in the quotient $\Delta t/\eta$ in Eq. 12). The point shown in **Figure 2** serves as a control point to monitor the evolution of the displacements in time.

A series of parametric studies was performed for η = 1, 10, 100, in order to examine the influence of the viscosity parameter η in the overall structure response. **Figure 3** shows typical results referring to the plastified area around the tunnel, in the supported, unsupported and tunnel front area, at the end of the analysis.

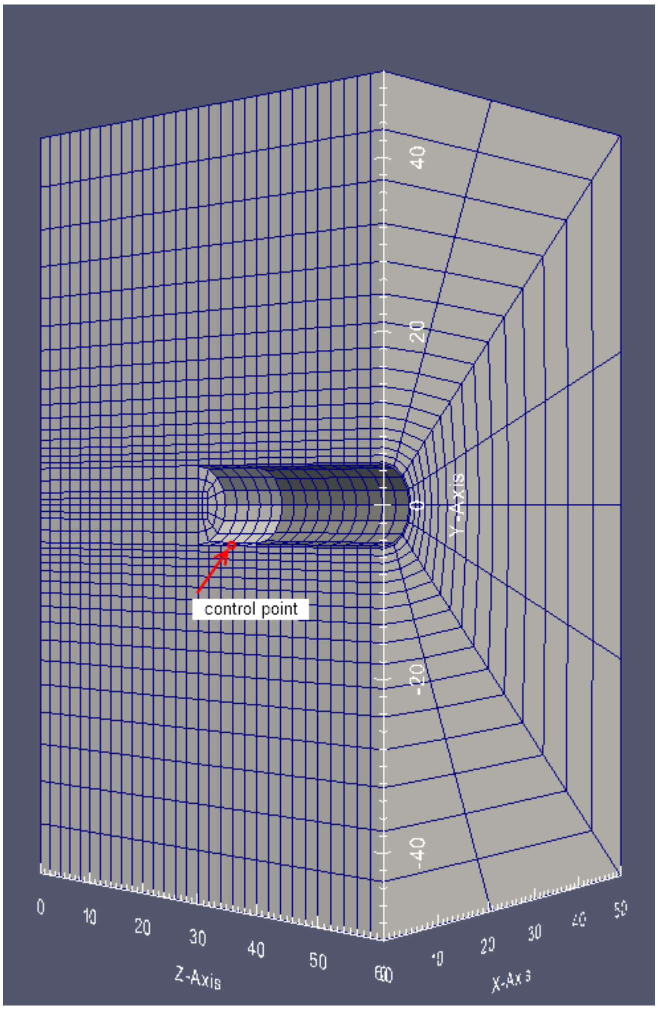

Figure 2. Finite element model.

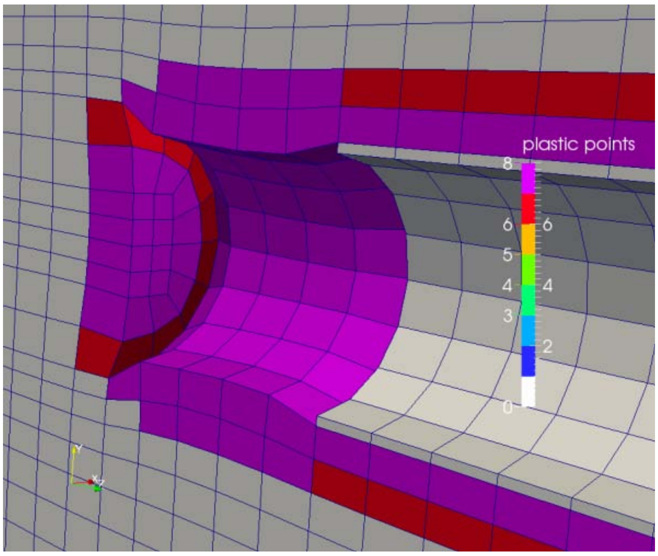

Figure 3. Plastified area.

According to the viscoplastic model assumed, displacements are evolved over time from the plastified regions, with a typical displacement field shown in **Figure 4**.

Finally in **Figure 5**, the evolution of radial displacements over time at the control point shown in **Figure 3** is presented. The influence of the viscosity parameter η over the displacements rate can be observed, where for smaller η the displacements convergence faster to the rate independent ones.

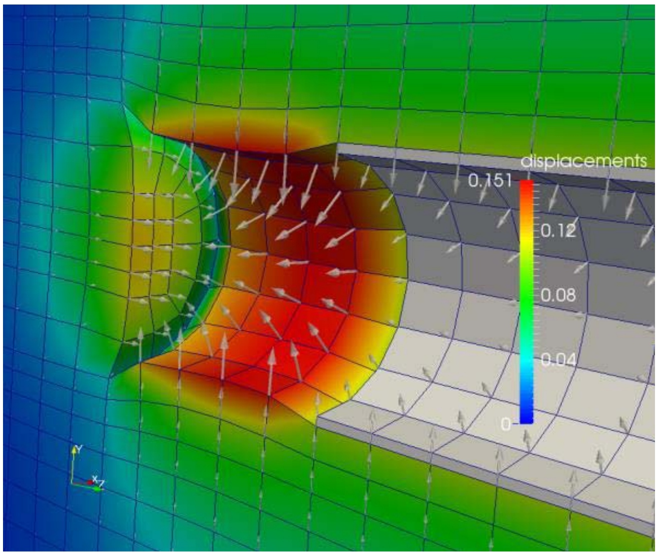

Figure 4. Displacements.

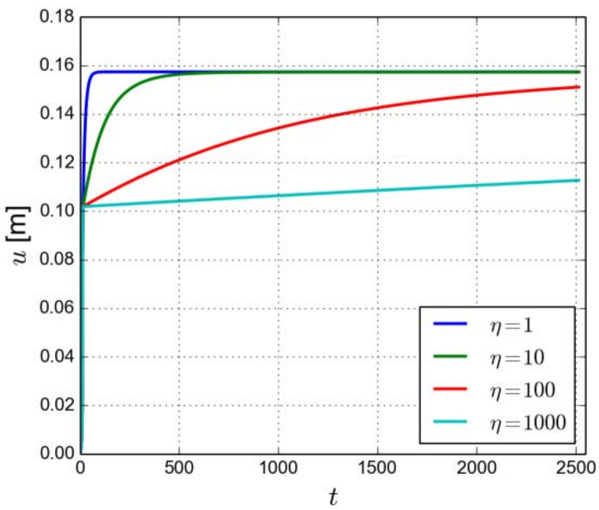

Figure 5. Displacements *vs* time for different values of the viscocity parameter η.

5 CONCLUSIONS

In this work the implementation of a viscoplastic model is presented, based on the well known Mohr-Coulomb criterion. Perfect plasticity is assumed to characterize the post-yield behavior, supplemented by a suitable generalization of the Duvaut-Lions viscoplastic model, used for the description of the corresponding rate-dependent behavior. The proposed model is implemented in a finite element code and applied to a typical tunnel excavation problem. The time evolution of the radial displacements for an unsupported part of the tunnel during construction is evaluated and used as a case study. Furthermore the influence of the viscosity parameter η in the overall structure response is examined through a series of parametric studies.

REFERENCES

Cristescu N. 1987, Elastic/Viscoplastic Constitutive Equations for Rock, *Int. J of Rock Mech and Min Sc & Geom Abs*, **24**, 271-282.

Cristescu N.D. & Hunsche U. 1998, *Time Effect in Rock Mechanics*, Wiley, New York.

Desai C.S. & Zhang D. 1987, Viscoplastic model for geologic materials with generalized flow rule, *Int J Numer Anal Met Geomech*, **11**, 603-620.

Datcheva M., Charlier R., & Collin F. 2001, Constitutive equations and numerical modelling of time effects in soft porous rocks, *Numerical Analysis and Its Applications*, **1988**, 1-21.

Duvaut G. & Lions J.L. 1976, *Inequalities in Mechanics and Physics*, Springer-Verlag.

Karaoulanis F.E. 2008, "Nonsmooth multisurface plasticity inprincipal stress space". *6th GRACM International Congress on* Computational Mechanics.

Karaoulanis F.E. 2009, "Implicit numerical integration of the Mohr-Coulomb surface in principal stress space". *2nd SE European Conference on Computational Mechanics*.

Karaoulanis F.E., 2009, An Efficient Algorithm for Non-smooth Multisurface Plasticity, *COMPLAS X, CIMNE*, Barcelona.

Karaoulanis F.E. 2010, *Multisurface elastoplastic yield criteria. Numerical implementation in principal stress space and application in Geotechnical Engineering problems*, PhD Thesis, Aristotle University of Thessaloniki.

Karaoulanis F.E. & Chatzigogos T. 2010, Numerical Solution of Multiple Yield Surfaces Elastoplastic Constitutive Models, *6th Hellenic Conference of Geotechnical and Geoenvironmental Engineering*.

Karaoulanis F.E. & Chatzigogos T. 2011. Elasto-viscoplastic modeling of soft rock time dependent behavior. *XV European Conference on SOIL Mechanics & Geotechnical Engineering*.

Karaoulanis F.E. 2013. *Implicit numerical integration of nonsmooth multisurface yield criteria in the principal stress space. Archives of Computational Methods in Engineering*, **20**, pp. 263-308.

Karaoulanis F.E., 2014. nemesis, *an experimental finite element code*, http://www.nemesis-project.org.

Koiter W.T. 1960, General Theorems for Elastic-plastic Solids. *Progress in Solid Mechanics* **6**, 167–221.

Moreau J.J. 1976, Application of Convex Analysis to the Treatment of Elastoplastic Systems, in *Applications of Methods of Functional Analysis to Problems of Mechanics*, Springer-Verlag, Berlin.

Owen D. R. J. & Hinton E. 1980, *Finite Elements in Plasticity: Theory and Practice*. Pineridge Press, Swansea, U.K.

Reed M.B. 1988, A viscoplastic model for soft rock*. Eng. Comput.* **5**, 65-70.

Simo J.C. & Hughes T.J.R. 1998, *Computational Inelasticity*, Springer-Verlag.

Sloan S.W. & Booker J.R. 1986, Removal of singularities in Tresca and Mohr-Coulomb yield functions. *Communications in Applied Numerical Methods*, **2**, 173-179.

Numerical investigation of the compression modulus of block-in-matrix pattern type geomaterials

Etude numérique du taux de compression des modèles matrice par blocs géomatériaux

F. E. Karaoulanis, S. Tsotsos

ABSTRACT The common practice for the estimation of the compressibility of geometerials resembling a block-in-matrix texture, is to assume that their compressibility is equal to the compressibility of the finer component of the matrix, which may lead to an overestimation of the predicted displacements. A numerical approach is adopted in this work in order to investigate the compression modulus of this type of geomaterials. A finite element model is employed to simulate a typical compression test. Then a series of Monte-Carlo simulations on the distribution of the blocks is performed. Finally, the results from the numerical tests are used to provide useful insight on the compressibility of block-in-matrix materials.

1 INTRODUCTION

Complex geological processes in nature may yield geomaterials with a strong heterogeneous structure, resembling a block-in-matrix texture. These materials are characterized by relatively significant rock blocks embedded in a matrix of finer materials. Typical examples of such materials can be found amongst others in residual soils, transported soils, fractured rocks and melánges.

The determination of the mechanical properties of block-in-matrix geomaterials is a challenging task. The common practice is to assume that their compressibility is equal to the compressibility of the finer component of the matrix, not taking into account the influence of the gravels, stones and/or other individual rock particles. This approach is introduced for convenience, as severe limitations in reliable sampling, in situ and laboratory tests, in addition to the complexity of the actual ground behavior, impose severe difficulties on the accurate modeling of their behavior. However, this oversimplified assumption is far from the real block-in-matrix compression mechanism and often becomes the cause of settlement overestimation.

In this article, a numerical approach is adopted in order to investigate the compression behavior of block-in-matrix pattern type geomaterials. A finite element model is employed to simulate a typical compression test. Then a series of Monte-Carlo simulations on the spatial distribution of the blocks is performed. Finally, the results from the numerical tests are used to provide useful insight on the compressibility of this type of geomaterials.

2 PROBLEM DESCRIPTION

Soil is the final product of *weathering* of unconsolidated rocks (fractured and/or weak). Two types of weathering are commonly recognized, namely mechanical and biogeochemical weathering, with the former being the process of physical disintegration of rock mass progressively into smaller particles, while the latter involves the decomposition of the rock and its chemical transformation (Mitcell and Soga 2005).

Continued weathering leads to the gradual formation of soil, usually seen in cross sections called *soil profiles* which reveal the soil horizons (van Breemen and Buurman 2002). A typical soil profile is given in Fig. 1, where the most common soil horizons are presented.

However, in nature various factors like nonuniformity of mechanical and chemical resistance of the rock mass combined with the aggressiveness and potential influence of the groundwater, may lead to deviations from this typical profile and to extremely complex geomaterials (Blight 1997).

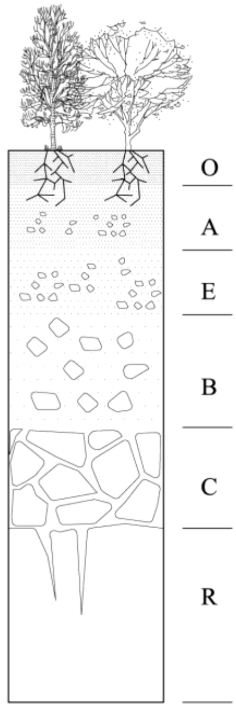

Figure 1. A typical soil profile (Soil Survey Division Staff, 1993).

2.1 Mixed Soils

Within this context the term mixed soils refers to those complex geomaterials consisting of rock fragments and soil. This type of geomaterials are commonly met in different scales in Geotechnical Engineering problems, including but not limited to residual soils, weathered rock fill materials or large scale breccia, also known as mélanges.

Mixed soils are characterized by a "block in matrix" pattern, where isolated interior rock blocks are embedded into a soil matrix. The strong spatial heterogeneity that mixed soils present, render sampling a tedious task (see Fig. 2), depending significantly on the available equipment and the personnel skills (Medley, 2001). As a result, characterization and geotechnical classification of mixed soils becomes significantly difficult and a reliable determination of the mechanical properties of these geomaterials is not always possible.

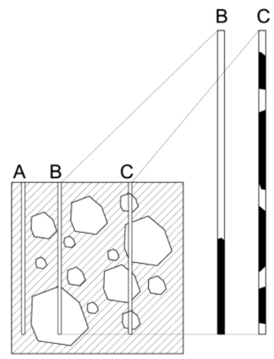

Figure 2. Difficulties in mixed soil sampling.

Therefore, it is common practice within the framework of Geotechnical Engineering to assume that the compressibility of the mixed soils is equal to the compressibility of the finer component of the mixture, not taking into account the influence of the individual rock particles. However, this oversimplified assumption is far from the real mixed soil compression mechanism and often becomes the cause of settlement overestimation. This work is focused on a more comprehensive approximation of mixed soil compressibility.

Geological structures consisting of rock particles embedded in a weaker soil material are frequently met in geology, resulting to over 1000 geological terms to describe them (Laznicka, 1998). Several classification systems have been proposed for the characterization and classification of this type of materials, mainly based on specific geological characteristics or their geological structure.

3.1 Classification

Wesley and Irfan (1997) propose a classification system for residual soils where the structure information is also considered. The Italian Geotechnical Association proposes a simple classification system for structurally complex formations, which covers amongst others, residual soils and mélanges (AGI, 1997). Raymond (1984) categorizes mélanges and similar rock formations and introduces the "block-in-matrix" term. Medley (1994) further extends this term into block-in-matrix rock or briefly *bimrocks*, which does not have any geological or geotechnical origin. According to Medley, bimrocks describe a mixture of rocks which consists of geotechnically significant blocks in a soil matrix. The notion of geotechnically significant mainly refers to the block size with respect to the size of the area of interest and in a lesser degree to the difference of the mechanical properties of the rock particles and the surrounding soil material.

3.2 Mechanical properties

Regarding the mechanical properties of mixed soils, several references can be found in the literature. Of great interest are the experimental works on mixed geomaterials consisting of rock particles in a clay matrix, subjected to unconsolidated undrained tests (Miller & Sowers, 1957), direct shear tests (Kurata & Fujishita, 1960) and consolidated drained tests (Kawakami & Abe, 1970). A further review of similar works can be found in (Lindquist, 1994).

Summarizing the outcome of the above mentioned works, it can be said that the friction angle significantly increases and the cohesion decreases when the percentage of the rock particles is above a threshold of 50% to 70%. This fact is explained according to Miller and Sowers (1957) by the formation of a skeleton by the rock particles. Irfan and Tang (1993) suggest that the friction angle should be increased by 30 for every 10% increment of the rock weight, within the range of 25% and 75%. Finally Lindquist, 1994, sets the maximum percentage limit to 85%-90%, above which the geomaterial should be considered as weathered rock.

Based on the above, it can be generally suggested for a mixed geometrical with a rock particle percentage r, that:

- If $r < 25\%$, then the behavior of the geomaterial is mainly governed by the matrix material.
- If $r > 75\%$, then the geometerial behavior is closer to that of a weathered rock.
- For $25\% < r < 75\%$, the geomaterial behavior is that of complex mixed soil.

Regarding the compressibility of the mixed soils, the related references in the literature are extremely limited. The authors have been studied several aspects of this problem and presented their work in a series of articles (Tsotsos *et al*., 2006; 2009; 2010).

More specifically, in Tsotsos *et al*., 2006, (see also Tsotsos *et al*., 2009) the problem is experimentally studied, by introducing two sets of artificial mixtures in scaled down samples consisting of different ratios of sand and clay. In this works, six different major categories are identified and proposed for the classification of mixed soils, namely:

- **Case 1**. The mixture consists only of soil (Fig. 3a); hence the compressibility of the mixture coincides with that of the soil.
- **Case 2**. Individual rock particles (gravels, aggregates, stones, boulders etc.) are scattered in the soil, surrounded by the soil, as shown in Fig. 3b.
- **Case 3**. The percentage of the granular particles is increased and thus some of them come into contact with each other (Fig.3c). The mechanism of deformation of the mixture in this case is complex, due to the complexity of the microstructure and the arrangement of the various grains.
- **Case 4**. The rocky parts occupy the largest area (Fig. 3d) and are in complete contact between them. All voids are filled with ground, implying that the void ratio is minimum in this case. The compressibility index of the mixture is now defined mainly by the compressibility of the evolving granular skeleton.
- **Case 5**. This case (Fig. 3e) differs from the previous one, as the soil material does not fill all the voids of the granular skeleton.
- **Case 6**. The mixture is a granular assemblage only (Fig. 3f). In nature, this case can be found in the case of fractured rocks.

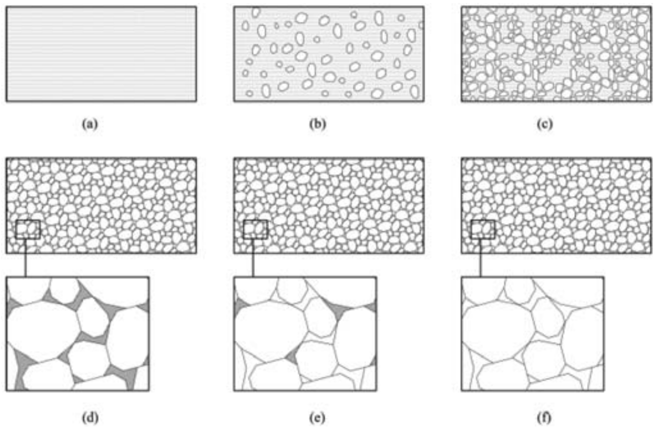

Figure 3. Representation of the sequential characteristic cases of clay sand mixtures with increasing sand content (Tsotsos et al, 2006, 2009).

Typical laboratory test results from the above works are shown in Fig. 4, where the compressibility index *Cc* is plotted against the clay percentage *a* of the mixture. It can be observed that the compressibility index in cases 1 and 6 coincides with the compressibility of the clay and sand respectively. Approaching case 4, as identified in Fig.3, the rate of the compressibility index is gradually decreased. In cases 2 and 3 the compressibility index is significantly reduced, as clay percent becomes lower. It is worth noticing that the reduction rate in the beginning is fairly large compared to the linear assumption of lines A and B, but is gradually decreased as we are moving from case 2 to case 4.

Similar were the findings when the problem was numerically approached by the authors using a series of Finite Element models. In Tsotsos *et al*., 2009 the above presented experimental work was modeled using axisymmetric conditions and the influence of the ratio of the two mixture components was studied. In Tsotsos *et al*., 2010 the influence of the block size was investigated, again under axisymmetric conditions. In both cases the findings are in accordance with the experimental work and strongly support the proposal of the 6 categories classification.

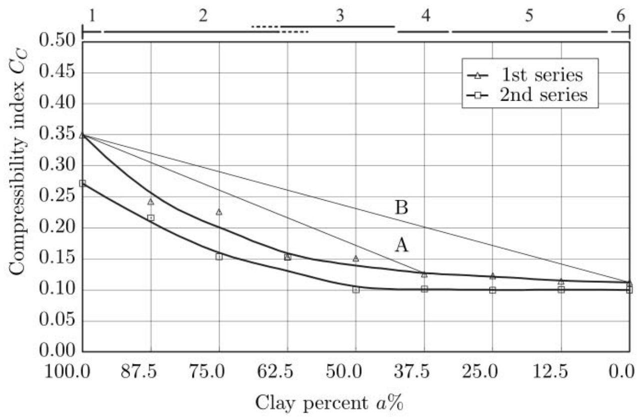

Figure 4. Compressibility index versus clay percent (Tsotsos et al, 2006, 2009). At the upper part of the figure the range of the six cases is given approximately.

In the current work a more elaborate Finite Element model is used in order to further investigate the compressibility behavior of mixed soils.

4 METHODOLOGICAL APPROACH

A series of numerical experiments are performed in a three dimensional finite element model, closely resembling the oedometer test. The finite element domain has dimensions of 75 × 20 mm and consists of 10307 nodes (30291 degrees of freedom) and 9120 eight node, displacement model hexahedral elements (see Fig. 5). The sizes of the finite elements are selected so that the mean volume of hexahedra used, equals to approximate 0.01% of the total volume.

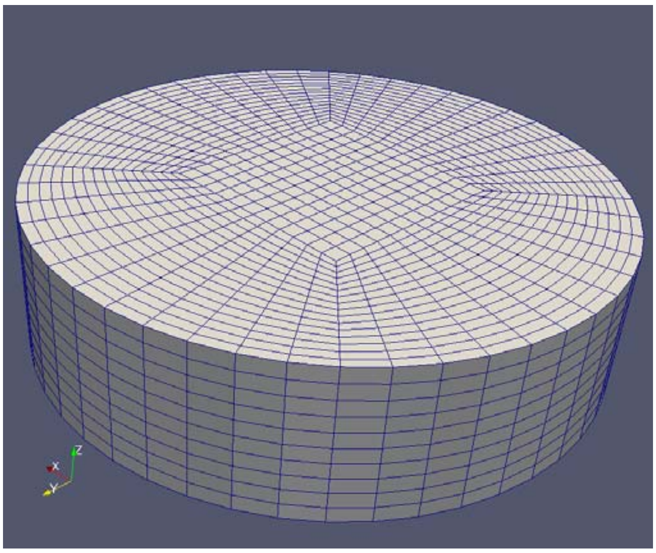

Figure 5. Finite element domain.

Either a stiff or a soft material is assigned in a random way to the elements, depending on the given prescribed ratio *r*, which refers to the volume percentage of the stiffer material. The ratio of the Young Modulus of the stiff material to the softer one is assumed to range within the set {5, 10, 25, 50, 100, 500, 1000, 10000}. These values correspond to a wide diversity of mixed geomaterials, ranging from the case of weak rock fragments in hard soil to the case of hard rock fragments in soft soil. The Poisson ratio is assumed equal to 0.25 for both materials. In Fig. 6 a typical snapshot of material assignment at different ratios *r* is plotted which lay for a ratio *r* equal to 15%. Both materials are assumed elastic and weightless.

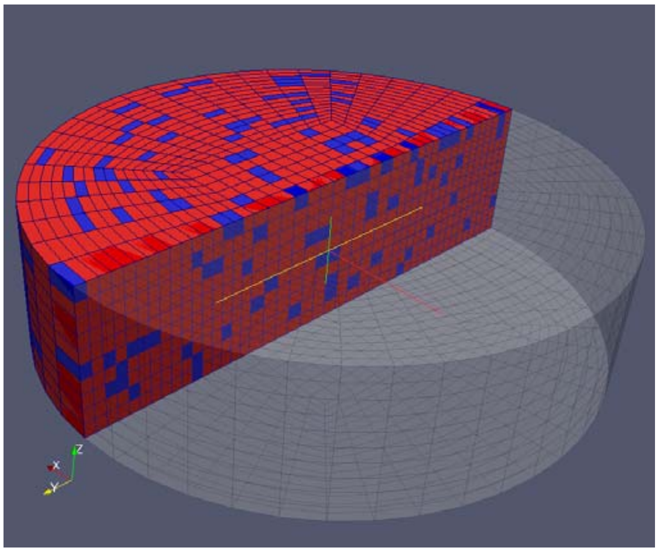

Figure 6. Typical material distribution for *r* = 15% (red: soft material, blue: stiff material).

The model is solved for a set of *a* values (0%, 5%, …, 50%), assuming 250 different mesh setups for each case and the top displacement is recorded. The behavior above *r* = 50% is assumed to be close to that of fractured rock (cases 4, 5 & 6) and is not considered to be captured adequately by the currently followed continuum approach. Special care is taken during the Monte Carlo experiments to avoid the formation of columns of stiff material, for higher values of *r*. Analyses are performed by the finite element code nemesis (Karaoulanis, 2014) which has been developed by the first author.

5 RESULTS

In Fig. 7 typical displacement results from a single analysis are presented, assuming *a* = 15%. The top average vertical strains from all analyses are shown in Fig. 8. The results are in overall agreement with the corresponding two dimensional analyses previously performed by the authors (Tsotsos *et al*, 2009). As it can be noticed, the top vertical strain of the mixture in all cases is smaller than the one that would result assuming homogeneity in the mixture, with the latter lying on a straight line connecting the starting and ending point of each curve. Furthermore this error is getting larger, as the second material is becoming stiffer.

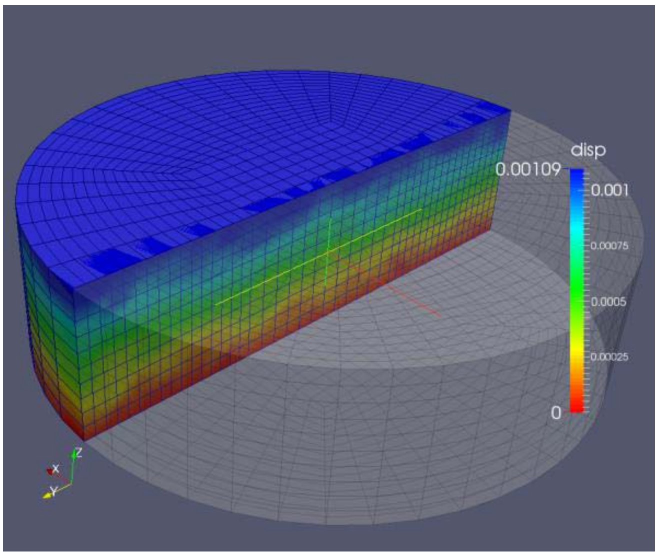

Figure 7. Displacements distribution for *r* = 15%.

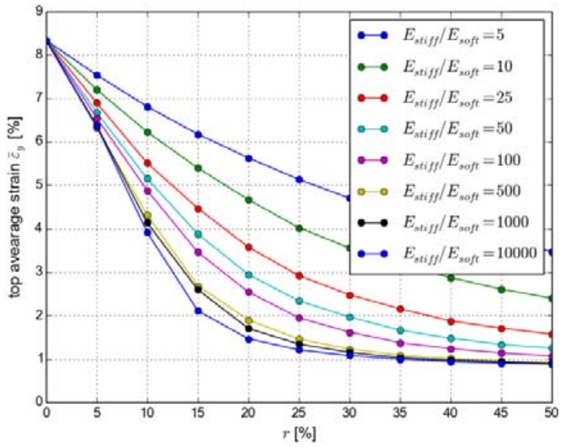

Figure 8. Top average vertical displacement.

Finally, the compression moduli ratio E_{mixed}/E_{soft} is plotted in Fig. 9, for the different cases of E_{stiff}/E_{soft}. Based on the above mentioned approach and the related assumptions, it can be concluded that the ratio E_{mixed}/E_{soft} ranges from 2 to 10 times, for $r < 50\%$.

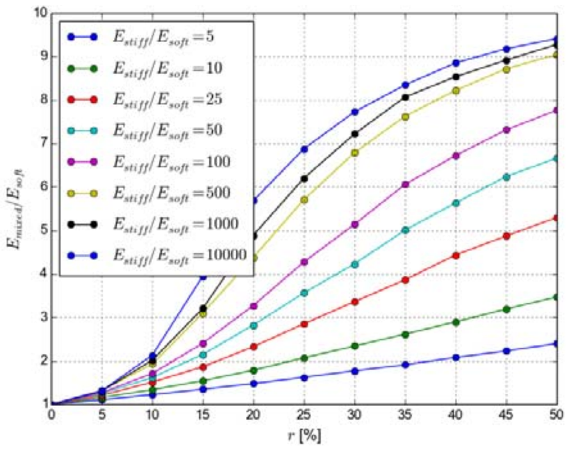

Figure 9. Ratio of E_{mixed}/E_{soft}.

6 CONCLUSIONS

The compressibility of mixed soils is studied numerically in this work, using a series of numerical tests based on a three dimensional finite element model. For the given assumptions and numerical results, the compression modulus of the block-in-matrix geomaterials can be properly defined, resulting in more realistic estimations of the overall displacements.

REFERENCES

Associazone Geotechnica Italiana, AGI 1997. *Proceedings of the International Symposium on the Geotechnics of Structurally Complex Formations.* Capri, Italy.

Blight G.E. 1997. Origin and formation of residual soils. In: Blight G.E. (ed) *Mechanics of residual soils*. Balkema, Rotterdam

Irfan T.Y. & Tang, K.Y. 1993. *Effect of the coarse fraction on the shear strength of colluvium*. Hong Kong Geotechnical Engineering Office, Report 15/92.

Kawakami H. & Abe H. 1970. Shear characteristics of Saturated Gravelly Clays. *Transactions of the Jap. Soc. Civil Eng.* **2**, 295-298.

Kurata S. & Fujishita T. 1960. Research on the Engineering Properties of Sand-Clay Mixtures. *Proc. 1st Asian Conf. Soil and Mechanics*, New Delhi, India **1**(**4**), 1-12.

Laznicka P. 1988. *Breccias and Coarse Fragmentites: Petrology, Environments, Ores.* Elsevier, Amsterdam, New York.

Lindquist E.S. 1994. *The Strength and Deformation Properties of Melange.* Ph.D. Thesis, University of California, Berkeley.

Medley, E.W. 1994. *The engineering characterization of mélanges and similar block-in-matrix rocks (bimrocks).* Ph.D. Thesis, University of California, Berkeley.

Medley E. 2001. Orderly Characterization of Chaotic Franziscan Mélanges. *FelsBau* **19** (**4**), 20-33.

Miller E.A. & Sowers G.F. 1957. The Strength Characteristics of Soil-Aggregate Mixtures. *Highway Research Board Bulletin* **183**, 6-23.

Mitchell J.K. & Soga K 2005. *Fundamentals of soil behavior*, 3rd edn. John Wiley & Sons

Karaoulanis F. E. 2014. *nemesis: an experimental finite element code*, http://www.nemesis-project.org.

Raymond, L.A. 1984. Classification of mélanges. Mélanges: Their nature, origin and significance. Raymond L.A. (ed.), *Geological Society of America*, Boulder, Colorado, Special Publication **228**, 7-20.

Soil Survey Division Stuff 1993. *Soil Survey Manual*. Soil Conservation Service. US Department of Agriculture. Handbook 18.

Tsotsos S., Grammatikopoulos I & Moditsis P. 2006. A study of the compressibility of composite geomaterials (rocky fragments surrounded by soil). *Proceedings, 5th Hellenic Conference of Geotechnical and Geoenviromental Engineering* **1**, 309-316.

Tsotsos S., Karaoulanis F.E. and Chatzigogos T. 2009. A New Concept on the Compressibility of Mixed Soils: Experimental and Numerical Approach. *Geotechnical and Geological Engineering* **28**, 199-207.

Tsotsos S., Karaoulanis F.E. & Chatzigogos T.N. 2010. Numerical simulation of mixed soil compressibility. Proceedings, 6th Hellenic Conference of Geotechnical and Geoenvironmental Engineering.

van Breemen N. & Buurman P. 2002. *Soil formation*, 2nd edn. Kluwer Academic Publishers

Wesley L.D. & Irfan T.Y. 1997. *Classification of Residual Soils. Mechanics of Residual Soils*, G.E. Blight (ed.), Balkema, Rotterdam, 17-29.

ΕΛΛΗΝΙΚΕΣ ΤΕΧΝΟΛΟΓΙΚΕΣ ΕΞΕΛΙΞΕΙΣ ΣΤΗΝ ΓΕΩΜΗΧΑΝΙΚΗ κ.α.

ΠΑΡΟΡΑΜΑ

Στην σελ. 26 του Τεύχους 86, Ιανουαρίου 2016 εγγράφη

(Ευάγγελος Παστρεμένης vastrin@crd.gr) αντί του ορθού (Ευάγγελος Αστρεινίδης, vastrin@crd.gr). Ζητούμε συγγνώμη από τον συνάδελφο για την παραποίηση του ονόματός του.

ΠΡΟΣΕΧΕΙΣ ΓΕΩΤΕΧΝΙΚΕΣ ΕΚΔΗΛΩΣΕΙΣ

Για τις παλαιότερες καταχωρήσεις περισσότερες πληροφορίες μπορούν να αναζητηθούν στα προηγούμενα τεύχη του «περιοδικού» και στις παρατιθέμενες ιστοσελίδες.

GeoAmericas 2016 3rd Panamerican Conference on Geosynthetics, 11 – 14 April 2016, Miami Beach, USA, www.geoamericas2016.org

International Symposium on Submerged Floating Tunnels and Underwater Structures (SUFTUS-2016), 20-22 April 2016, Chongqing, China, www.cmct.cn/suftus

World Tunnel Congress 2016 "Uniting the Industry", April 22-28, 2016, San Francisco, USA, http://www.wtc2016.us

International Symposium "Design of piles in Europe - How did EC7 change daily practice?", 28-29 April 2016, Leuven, Belgium, www.etc3.be/symposium2016

7th In-Situ Rock Stress Symposium 2016 - An ISRM Specialised Conference, 10-12 May 2016, Tampere, Finland, www.rs2016.org

84th ICOLD Annual Meeting, 15-20 May 2016, Johannesburg, South Africa, www.icold2016.org

Infrastructure Summit 2016, 18 - 19 May 2016, London, United Kingdom, Ilya.Ryndin@emap.com

2nd International Conference on Rock Dynamics and Applications (RocDyn-2), 18 – 20 May 2016, Suzhou, China http://rocdyn.org

6th Annual Underground Infrastructure and Deep Foundations Qatar, 23–24 May 2016, Doha, Qatar, oliver.osea@iqpc.ae

13th International Conference Underground Construction Prague 2016 and 3rd Eastern European Tunnelling Conference (EETC 2016), 23 to 25 May 2016, Prague, Czech Republic, www.ucprague.com

GEOSAFE: 1st International Symposium on Reducing Risks in Site Investigation, Modelling and Construction for Rock Engineering - an ISRM Specialized Conference, 25 – 27 May 2016, Xi'an, China, www.geosafe2016.org/dct/page/1

14th International Conference of the Geological Society of Greece, 25-27 May, Thessaloniki, Greece, www.ege2016.gr

NGM 2016 - The Nordic Geotechnical Meeting, 25 - 28 May 2016, Reykjavik, Iceland, www.ngm2016.com

International Mini Symposium Chubu (IMS-Chubu) New concepts and new developments in soil mechanics and geotechnical engineering, 26 - 28 May 2016, Nagoya, Aichi, Japan, www.jiban.or.jp/index.php?option=com_content&view=article&id=1737:2016052628&catid=16:2008-09-10-05-02-09&Itemid

11th HSTA< International Congress on Mechanics – Mini-Symposium Computational Geomechanics from Micro to Macro, May 27-30, 2016, Athens, Greece, http://11hstam.ntua.gr

19SEAGC – 2AGSSEAC Young Geotechnical Engineers Conference, 30th May 2016, Petaling Jaya, Selangor, Malaysia, seagc2016@gmail.com

19th Southeast Asian Geotechnical Conference & 2nd AGSSEA Conference Deep Excavation and Ground Improvement, 31 May – 3 June 2016, Subang Jaya, Malaysia, seagc2016@gmail.com

ISSMGE TC211 Conference Session within the framework of the 19th Southeast Asian Geotechnical Conference "GROUND IMPROVEMENT works: Recent advances in R&D, design and QC/QA"

ISL 2016 12th International Symposium on Landslides Experience, Theory, Practice, Napoli, June 12th-19th, 2016, www.isl2016.it

2ο Πανελλήνιο Συνέδριο
Εξόρυξης και Εναλλακτικών Μεθόδων Διαχείρισης Αποβλήτων
15-16 Ιουνίου 2016, Αθήνα
www.erasmus.gr/microsites/1091

Το πρόγραμμα του Συνεδρίου θα περιλαμβάνει ομιλίες και παρουσιάσεις, με βασικά θέματα την Εξόρυξη Αποβλήτων, τα αποτελέσματα του Έργου LIFE+ reclaim, καθώς και τη Διαχείριση των Στερεών Αποβλήτων και των Χώρων Διάθεσής τους, όπως και εναλλακτικές μεθόδους διαχείρισης των αποβλήτων. Κατά τη διάρκειά του, αναμένεται να λάβουν χώρα ενδιαφέρουσες συζητήσεις από ειδικούς και ενδιαφερόμενους στα θέματα της διαχείρισης αποβλήτων, σχετικά με τα οφέλη και τις προοπτικές εφαρμογής εναλλακτικών μεθόδων διαχείρισης.

Στο Συνέδριο θα πραγματοποιηθούν ομιλίες και παρουσιάσεις, στο πλαίσιο της παρακάτω θεματολογίας:

- Διαχείριση Αστικών Αποβλήτων
- Εξόρυξη Αποβλήτων
- Καινοτόμες Προτάσεις Διαχείρισης Αποβλήτων
- Νέες Τεχνολογίες και Εναλλακτικές Μέθοδοι στη Διαχείριση Αποβλήτων
- Αποκατάσταση Χώρων Διάθεσης Αποβλήτων

Η συμμετοχή στο συνέδριο είναι ΔΩΡΕΑΝ

Γραμματεία Οργάνωσης
Erasmus Conferences Tours & Travel S.A.
Κολοφώντος 1 & Ευρυδίκης, 161 21 Αθήνα
Τηλ: 210 7414700 • Φαξ: + 30 210 7257532
E-mail: register@erasmus.gr • Website:www.erasmus.gr

BCRRA 2017 Tenth International Conference on the Bearing Capacity of Roads, Railways and Airfields, 28 –30 June 2017, Athens, Greece, www.bcrra2017.com

ICONHIC 2016 1st International Conference on Natural Hazards and Infrastructure: Protection, Design, Rehabilitation, 28-30 June 2016, Chania, Greece, http://iconhic2016.com

ICONHIC 2016 Performance-based soil-structure interaction of lifelines and infrastructure, gerolymos@gmail.com, asextos@civil.auth.gr & a.sextos@bristol.ac.uk

4th GeoChina International Conference Sustainable Civil Infrastructures: Innovative Technologies for Severe Weathers and Climate Changes, July 25-27, 2016, Shandong, China, http://geochina2016.geoconf.org

S3: Slopes, Slides and Stabilization, August 1-3, 2016, Denver, USA, events@dfi.org

6th International Conference on Recent Advances in Geotechnical Earthquake Engineering and Soil Dynamics August 1-6, 2016, Greater Noida (NCR), India, www.6icragee.com

EUROC 2016 - ISRM European Regional Symposium Rock Mechanics & Rock Engineering: From Past to the Future, 29-31 August 2016, Ürgüp-Nevşehir, Cappadocia, Turkey http://eurock2016.org

ICEGE 2016 1st International Conference on Energy Geotechnics, 29-31 August 2016, Kiel, Germany, www.iceg-2016.de

3rd ICTG – 3rd International Conference on Transportation Geotechnics 4 - 7 September 2016, Guimaraes, Portugal, www.civil.uminho.pt/3rd-ICTG2016

IAS'5 5th International Conference on Geotechnical and Geophysical Site Characterisation, 5-9 September 2016, Gold Coast, Queensland, Australia, http://www.isc5.com.au

The World Multidisciplinary Earth Sciences Symposium–WMESS 2016, 5-9 September 2016, Prague, Czech Republic www.mess-earth.org

ACCUUS 2016 15th World Conference Underground Urbanisation as a Prerequisite for Sustainable Development, September 12-15, 2016, http://acuus2016.com

SAHC 2016 - 10th international Conference on Structural Analysis of Historical Constructions 13-15 September 2016, Leuven, Belgium, www.sahc2016.be

13 Baltic States Geotechnical Conference Historical Experiences and Challenges of Geotechnical Problems in Baltic Sea Region, 15 - 17 September 2016, Vilnius, Lithuania, http://www.13bsgc.lt

ACE 2016 12th International Congress on Advances in Civil Engineering, 21-23 September 2016, Istanbul, Turkey, http://www.ace2016.org

EuroGeo 6 – European Regional Conference on Geosynthetics, 25 – 29 Sep 2016, Istanbul, Turkey, www.eurogeo6.org

8th Nordic Grouting Symposium State of the art – Future Development, 26-27 September 2016, Oslo, Norway, http://nordicgrouting.com

5th International Scientific Conference on Industrial and Hazardous Waste Management, 27 - 30 September 2016, Chania, Crete, Greece, http://hwm-conferences.tuc.gr

2nd International Specialized Conference on Soft Rocks – ISRM 2016 Understanding and interpreting the engineering behavior of Soft Rocks, 6-7 October 2016, Cartagena, Colombia, www.scg.org.co/?p=1634

ARMS 9, 9th Asian Rock Mechanics Symposium, ISRM Regional Symposium, 18-20 October 2016, Bali, Indonesia, http://arms9.com

SFGE 2016 Shaping the Future of Geotechnical Education International Conference on Geo-Engineering Education 20 - 22 October 2016, Minascentro, Belo Horizonte, MG, Brazil, http://cobramseg2016.com.br/index.php/sfge-sobre/?lang=en

10th ICOLD European Club Symposium & Exhibition, 25-30 October 2016, Antalya, Turkey, http://trcold.com

NEMO International Conference Probing the Santorini volcano for 150 years / Διεθνές συνέδριο NEMO 150 χρόνια μελέτης ηφαιστείου της Σαντορίνης, 3-5 November 2016, Santorini, Greece, http://nemo.conferences.gr

GeoAsia 6 - 6th Asian Regional Conference on Geosynthetics 8-11 November 2016, New Delhi, India, http://seags.ait.asia/news-announcements/11704

RARE 2016 Recent Advances in Rock Engineering 16-18 November 2016, Bangalore, India, www.rare2016.in

TBM DiGs Istanbul 2016 2nd International conference on "TBM DiGs in difficult grounds", 16-18 November 2016, Istanbul, Turkey, www.tbmdigsturkey.org

International Symposium on Submerged Floating Tunnels and Underwater Tunnel Structures (SUFTUS-2016), 16—18 December 2016, Chongqing, China, www.cmct.cn/suftus

AfriRock 2017, 1st African Regional Rock Mechanics Symposium, 12 – 17 February 2017, Cape Town, South Africa, www.saimm.co.za/saimm-events/upcoming-events

World Tunnel Congress 2017 Surface challenges – Underground solutions, 9 to 16 June 2017, Bergen, Norway, www.wtc2017.no

EUROCK 2017 Human Activity in Rock Masses, 13-15 June 2017, Ostrava, Czech Republic, www.eurock2017.com

GeoMEast2017, 15 - 19 July 2017, Sharm El-Sheik, Egypt, www.geomeast2017.org

19th International Conference on Soil Mechanics and Geotechnical Engineering, 17 - 22 September 2017, Seoul, Korea, www.icsmge2017.org

BCRRA 2017 Tenth International Conference on the Bearing Capacity of Roads, Railways and Airfields, 28th to 30th June 2017, Athens, Greece, www.bcrra2017.com

GeoAfrica 2017
3rd African Regional Conference on Geosynthetics
9 – 13 October 2017, Morocco

11th International Conference on Geosynthetics (11ICG)
16 - 20 Sep 2018, Seoul South Korea
csyoo@skku.edu

ꕥ ꕥ

10th Asian Rock mechanics Symposium - ARMS10
October 2018, Singapore

Prof. Yingxin Zhou
Address:
1 Liang Seah Street
#02-11 Liang Seah Place
SINGAPORE 189022
Telephone: (+65) 637 65363
Fax: (+65) 627 35754
E-mail: zyingxin@dsta.gov.sg

ꕥ ꕥ

AFTES International Congress "The value is Underground"
13-16 November 2017, Paris, France

ꕥ ꕥ

World Tunnel Congress 2018
20-26 April 2018, Dubai, United Arab Emirates

ꕥ ꕥ

EUROCK 2018
22-26 May 2018, Saint Petersburg, Russia

Contact Person: Prof. Vladimir Trushko
Address: 21-st line V.O., 2
199106 St. Petersburg
Russia
Telephone: +7 (812) 328 86 71
Fax: +7 (812) 328 86 76
E-mail: trushko@spmi.ru

ꕥ ꕥ

UNSAT2018 The 7th International Conference on Unsaturated Soils, 3 - 5 August 2018, Hong Kong, China, www.unsat2018.org

ꕥ ꕥ

ARMS10
10th Asian Rock Mechanics Symposium
ISRM Regional Symposium
October 2018, Singapore

Contact Person: Prof. Yingxin Zhou
Address: 1 Liang Seah Street
#02-11 Liang Seah Place
SINGAPORE 189022
Telephone: (+65) 637 65363
Fax: (+65) 627 35754
E-mail: zyingxin@dsta.gov.sg

ꕥ ꕥ

14th ISRM International Congress
2019, Foz de Iguaçu, Brazil

Contact Person: Prof. Sergio A. B. da Fontoura
E-mail: fontoura@puc-rio.b

ΕΝΔΙΑΦΕΡΟΝΤΑ ΓΕΩΤΕΧΝΙΚΑ ΝΕΑ

Οι πιο εντυπωσιακοί σταθμοί μετρό στον κόσμο Από τη Μόσχα και τη Λισαβόνα μέχρι το Μόντρεαλ και την Τασκένδη

Τα πιο ιδιαίτερα μετρό στον κόσμο, τα οποία αποτελούν αξιοθέατα από μόνα τους.

Μόσχα, Ρωσία

Κάτω από το Κρεμλίνο και την Κόκκινη Πλατεία, εκεί όπου το φως του ήλιου δεν φτάνει ποτέ, κρύβεται ένα τεράστιο δίκτυο υπόγειας τέχνης. Είναι το μετρό της Μόσχας, με σταθμούς που συναγωνίζονται τα μουσεία της. Θ' ακούσετε να τους αποκαλούν «παλάτια για τους ανθρώπους». Τ' ανάγλυφα αετώματα, οι μεγαλοπρεπείς τοιχογραφίες, μέχρι και πολυέλαιοι-υπερπαραγωγή, μπορούν να σε κάνουν να ξεχάσεις ποιο συρμό θέλεις να πάρεις. Must είναι ο σταθμός Kievskaya (για τα μωσαϊκά του) και ο σταθμός Novoslobodskaya (για τα υπέροχα βιτρό του).

Λισαβόνα, Πορτογαλία

Όποια γραμμή και αν επιλέξεις, είναι ένα ταξίδι στην ιστορία των azulejos (έτσι λένε τα πολύχρωμα κεραμικά πλακάκια). Και οι 46 σταθμοί του παίζουν με αυτήν την πρώτη ύλη έχοντας τόσο διαφορετικά αποτελέσματα. Λένε πως ο «βασιλιάς» των σταθμών είναι ο Olaias, καθώς συνδυάζει την ιδιαίτερη αρχιτεκτονική του Tomas Taveira και τα έργα καλλιτεχνών αγαπημένων στην πόλη, σε μια πραγματική έκρηξη χρωμάτων. Να σημειωθεί, παρακαλώ, ότι αυτή η τεχνοτροπία με τα πλακάκια ξεπέρασε τα σύνορα της χώρας κι έφτασε πλέον να διακοσμεί τους σταθμούς του μετρό στις Βρυξέλλες, στο Παρίσι, στη Βουδαπέστη, στη Μόσχα και στο Σίντνεϊ

Στοκχόλμη, Σουηδία

Τα 108 χιλιόμετρα σήραγγας έχουν το παρατσούκλι «η εκτε-

νέστερη γκαλερί τέχνης στον κόσμο». Ενενήντα από τους 101 σταθμούς είναι διακοσμημένοι με πολύχρωμα έργα τέχνης που κατά καιρούς αλλάζουν. Εκατόν σαράντα καλλιτέχνες έχουν βάλει την προσωπική τους σφραγίδα, κάνοντας το μετρό της Στοκχόλμης ένα από τα πιο διάσημα αξιοθέατά της. Οι επιβάτες της μπλε γραμμής βιώνουν κάθε μέρα μια μυστηριώδη εμπειρία που δύσκολα συνηθίζεται. Οι σταθμοί είναι φτιαγμένοι σαν μεταμοντέρνα σπήλαια, από χρωματιστή πέτρα, με ζωηρούς πίνακες, χρυσά μωσαϊκά και κατασκευές που κρέμονται από το ταβάνι. Εμπνευστής είναι ο Per Olof Ultvedt, το καλύτερο έργο του οποίου βρίσκεται στο σταθμό T-Centralen.

Βερολίνο, Γερμανία

Η Σουηδία έχει δώσει ένα χεράκι και στο Βερολίνο. Οι εβδομήντα σταθμοί που έφτιαξε ο Σουηδός αρχιτέκτονας Alfred Grenander έκαναν αυτόματα την υψηλή αρχιτεκτονική προνόμιο των πολλών. Το ντιζάιν των πιο καινούργιων σταθμών (δημιουργήματα του Rainer G. Rümmler αυτοί) είναι ένας ύμνος στο ρεύμα του μινιμαλισμού της δεκαετίας του '60, της ποπ αρτ του '70 και του μεταμοντερνισμού.

Λιλ, Γαλλία

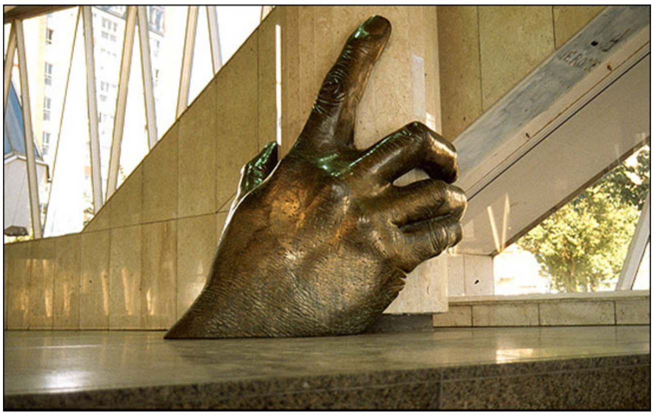

Εντάξει, το μετρό στο Παρίσι με τους αρ νουβό σταθμούς είναι σίγουρα ένα νοσταλγικό ταξίδι σε άλλη εποχή. Ωστόσο, αυτό που κέρδισε τη δική μας προτίμηση είναι της Λιλ, το πρώτο σύστημα μετρό στον κόσμο χωρίς οδηγό. Εγκαινιάστηκε το 1983 και σχεδόν όλοι οι σταθμοί έχουν δική τους καλλιτεχνική προσωπικότητα. Κάπου μπορεί να βρείτε μια πισίνα που τα νερά της αντανακλούν τη «φευγάτη» αρχιτεκτονική, κάπου αλλού ενυδρεία με ψάρια. Οι περισσότεροι, πάντως, σταματούν στο Porte de Valenciennes για να δουν το τεράστιο χέρι που κρατάει τις κολόνες του σταθμού, ένα έργο του διάσημου γλύπτη César.

Μόντρεαλ, Καναδάς

Très intéressant, n'est-ce pas? Στη γαλλόφωνη μεγαλούπολη δεν ήθελαν ένα απλό μετρό. Από το 1966 μεταμορφώνουν όλους τους σταθμούς σ' ένα παράλληλο σύμπαν με μεταλλικά αγάλματα, εντυπωσιακά μωσαϊκά, βιτρό και τοιχογραφίες. Και το τρένο να μην υπήρχε, οι σταθμοί θα είχαν ζωή. Εκατόν πενήντα έργα –και βάλε– σύγχρονης τέχνης κοσμούν το μετρό του Μόντρεαλ. Highlight ο σταθμός του Monk με τα τεράστια (σχεδόν διώροφα!) μεταλλικά αγάλματα του Germain Bergeron.

Τασκένδη, Ουζμπεκιστάν

Δεν είναι αστείο! Στο Ουζμπεκιστάν βρίσκεται ένα από τα πιο αριστοκρατικά μετρό του κόσμου. Όλη η πρώην Σοβιετική Ένωση το θεωρεί μνημείο ανεκτίμητης αξίας. Από το 1977 και μετά, οι πιο αναγνωρισμένοι ντόπιοι αρχιτέκτονες και καλλιτέχνες χρησιμοποίησαν γυαλί, γρανίτη, μάρμαρο και σκαλισμένο αλάβαστρο, με αποτέλεσμα το μετρό να προσελκύει περισσότερους επισκέπτες, οι οποίοι έρχονται για να το θαυμάσουν ως αξιοθέατο και όχι για να κινηθούν στην πόλη! Το ταβάνι με τους φωτεινούς θόλους και τα ισλαμικά σχέδια του σταθμού Navoiy τα συμπεριλαμβάνουμε κι επισήμως ανάμεσα στα ωραιότερα που έχουμε δει.

(Δημήτρης Βγενής Φαλλιέρος / ΑΘΗΝΟΡΑΜΑ, 15.02.2016 http://www.athinorama.gr/travel/travelideas/articles.aspx?artid=2511873&utm_source=TravelThema6&utm_medium=newsletter&utm_campaign=Travel_newsletter_2016-2-15)

The greatest ever debris flow video? Aconcagua in Argentina

This one, on the flanks of Aconcagua in Argentina, is quite spectacular. It starts slowly, but hang in there!

https://www.youtube.com/watch?v=jNVwspunNn0

The original text accompanying the video is in Spanish, a tidied up Google Translation version is as follows:

"Avalanche between Horcones (park entrance) and Confluence (first base camp of the Aconcagua field). Julian Insarralde [who posted the video], Nico Aguero and Naco Choulet were working for INOUT ADVENTURE during a trek lasting three days. We are going to customers to avoid them being splashed with mud as it is an area of avalanches at that time of year. The warning was a sound similar to an airplane sound, which is why Julian Insarralde is looking back and is able to warn that an avalanche is coming. That's why we ran and we did not abandon people so that we were in the safe zone. They are things that can happen when we work in real natural environments".

This is the moment that the debris flow arrives:-

This is a classic debris flow – the front end is almost entirely dry (note the dust in the image above) and mostly large boulders. The tail of the debris flow has more water and finer material. Note that the debris flow goes through a series of surges.

The weather appears to be dry and sunny. The very small debris flow that the hikers are crossing at the start is also quite intriguing. Even this appears to be debris rich. I wonder if this is the tail of an earlier surge? The walls of the gully appear to be wet?

Its a pretty good job that the trekkers heard the debris flow coming, and respect to everyone for getting out of the way, despite a couple of slips and trips.

(24 January 2016, http://blogs.agu.org/landslideblog/2016/01/24/the-greatest-ever-debris-flow-video-aconcagua/)

Yaglidere – a dramatic landslide video from Turkey

This video was posted on Youtube (σ.ε. έχει αποσυρθή από το youtube) on 11th February 2016. It appears to have occurred at Yaglidere in Giresun, Turkey. The comments that accompany it are in Turkish

Into a fragmented highly mobile mass in just a couple of seconds:

The displacement of the water in the river is certainly impressive. The landslide appears to be in fine grained silts or sands – possibly loess? I cannot find any information about the superficial geology of Giresun.

(17 February 2016, http://blogs.agu.org/landslideblog/2016/02/17/yaglidere/)

An update on the Yaglidere Landslide, including another video

Yesterday I blogged about the Yaglidere landslide. I have tracked down a second video on Youtube in some ways even more dramatic than the original:

The video of the Yaglidere landslide was posted on the website of the Yaglidere Gazette (I'm sure you are all avid readers already), who also has a news report (in Turkish) about the landslide, which includes this image of the aftermath:
https://www.youtube.com/watch?v=v71fiW9436k#t=77

The following image shows that the landslide was on the outside of a river bend. It appears that there might have been some works going on at this site prior to the failure, but this may have been clearance of the debris from earlier landslides.

Yaglidere landslide via the Yaglidere Gazette

Caner Zanbak via a comment on my original post has very kindly provided this information:

The landslide referred in the video at Yaglıdere, Giresun, Turkey occured on 4 February, 2016 following quick melt of accumulated snow by heavy rainfall events. Based on the information provided by engineering geologist Assoc. Prof. Hakan Ersoy (ersoy@ktu.edu.tr) of Karadeniz Technical University in Trabzon, Turkey, surface morphology at the landslide area reveals likely presence of large-scale paleo-landslide mass overlying the highly weathered (exfoliated, arenaceous, argillaceous) intrusions of the upper Cretaceous Kaçkar Granitoids. The recent landslide has taken place in the paleo-landslide mass.

As seen in the related video showing the ultimate failure, the landslide was triggered by the earlier erosion of the natural slope toe by the river and progressed upwards under a combination of inclined base and pseudo-circular failure mode. The height of the near vertical exposed slide surface is approximately 20 meters. Please note that another slope on the left side of the current landslide is prone to a similar failure.

(18 February 2016, http://blogs.agu.org/landslideblog/2016/02/18/yaglidere-landslide-1/)

AGU : American Geophysical Union

10 roads you would never want to drive on

https://www.youtube.com/watch?v=ym4uVS-5tSA

Since the invention of the modern automobile, we have been in love with our cars, trucks and motorcycles. It's hard to think how we could function on a daily basis without a personal car around to take us to the grocery store, movie theatre or over to a friend's house. This mode of transportation is such an important part of most peoples' lives that we have no idea how we'd cope if cars suddenly disappeared tomorrow. Sure, most cars pollute and after a decade or so we get rid of the old and bring in a new car – filling up wrecking yards and burnings tons of gasoline in the process. The automobile is so important that rather than develop a whole new mode of transportation we instead focus our energy on creating more efficient gasoline burning engines and new models of electric cars. Nonetheless, the car is an integral part of our lives and our culture.

Of course, many people have often heard the saying (but never really payed any attention to it) that driving is one of the most dangerous things we do in our daily lives. Indeed, getting behind the wheel of your ride and heading off to work or some other destination can be very dangerous. Statistically, the number crunchers say that you are far more likely to die driving your car than flying in a plane. The numbers seem to back this up by showing that over 90 people are killed every day in motor vehicle accidents in the US alone. It all makes sense once you think about it. If you think about all the people out on the road and add in distracted and drunk drivers, mechanical failures and bad weather then it's easy to see why driving can be so dangerous.

But what about the actual sections of roads and highways that seemingly have a high number of accidents and fatalities all year round. That is, it can be bad enough driving on 'regular' roads and highways around the world but there are roads which, for whatever reason, just seem more dangerous than the rest. You are probably picturing the classic mountain side road, carved into the rock with minimal safety barriers and exposed to landslides and all the inclement weather you can think of. Yes, those roads are very dangerous, but they aren't the only ones to avoid driving on. As part two of our 'dangerous roads' series, we look at 10 roads you probably wouldn't want to drive on. These motorways are found all across the world, in all sorts of environments and at all sorts of altitudes. There are the expected mountain roads – narrow and crumbling where one small mistake means you are going for a very long fall. There are also the remote and isolated highways running through deserts and the vastness of Siberia. There are even the sea level roads which provide their own nasty little surprise that can ruin your day (or life). We guarantee that after seeing this your daily commute will appear to be a walk in the park.

ΕΝΔΙΑΦΕΡΟΝΤΑ - ΠΕΡΙΒΑΛΛΟΝ

Polyaromatic Hydrocarbon Compounds; Avoiding High Disposal Costs and Appropriate Reuse of Road Planings

Why are Road Planings Difficult Materials?

Many of Britain's urban roads were constructed prior to the 1980s and are now subject to repair/replacement. This can involve a complete new pavement construction or the planing off of the upper wearing course, and its replacement with a new surface. The volume of bound aggregate or planings generated by such works can be significant. Any road surface constructed before the 1980s, or any roads surface dressed to the end of the late 1980s could contain coal tar as a binder for the aggregate.

Coal tar is rich in polyaromatic/polycyclic hydrocarbons and is a potentially hazardous material manufactured from by-products of former 'town' gas works and was used as a binder or as spray coating in road construction due to its good adhesive and water-proofing properties. In the late 1970s/early 1980s, the use of coal tar faded out with the closure of the town gas works and it was replaced with bitumen which is manufactured from oil products, and is a less hazardous material.

In addition to tar, tar oil flux was used to aid workability of some macadam, and pitch was derived from coal tar for use in hot rolled asphalt surfacing in the 1960s and 1970s.

What are and why are PAHs Important?

Polyaromatic/polycyclic hydrocarbon (PAH) compounds are a group of organic compounds commonly found on brownfield sites, but also occur naturally. They comprise over one hundred compounds which all share the same basic building block, a series of benzene rings fused together, as shown on the figure to the left (the hexagons in the figure each represent one benzene ring), but all have different physical and chemical properties which influence their potential to cause harm to human health and the environment. Naphthalene with two rings is the simplest PAH compound.

The compounds are commonly created as a by-product of the incomplete combustion of organic material, and are not only found on contaminated land. They are present in cigarette smoke, from vehicle emissions and atmospheric fallout on otherwise 'greenfield' sites. PAH compounds were first studied in the late 19th and early 20th centuries, when they were identified as the cause of cancers within people working with coal tars, and it has since been observed that their effects can be carcinogenic and mutagenic. The US Environmental Protection Agency (EPA) designated 16 PAH compounds which were commonly found on brownfield sites, but also were the most likely to pose a risk to human health or the environment. Other authorities have selected other groups of compounds for their own purposes (e.g. 22 compounds by the UKSHS) however the US EPA 16 PAH compounds form the basis of most analyses.

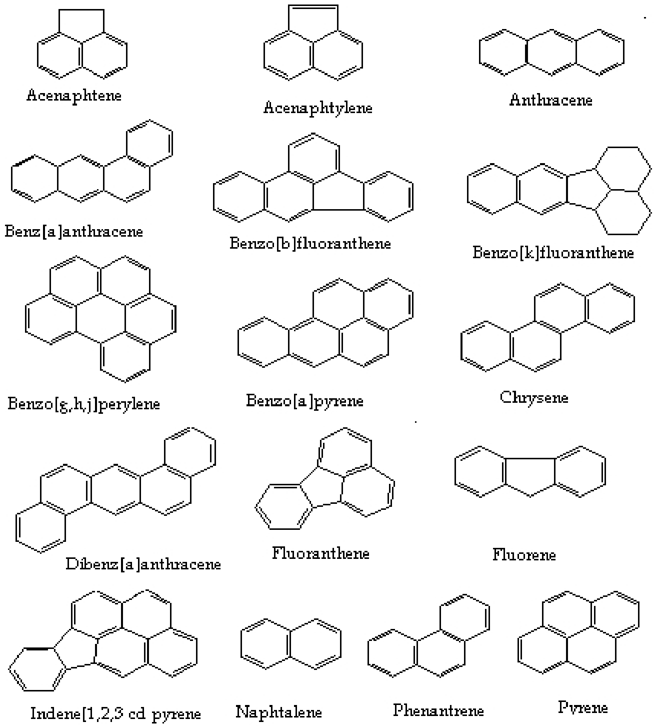

PAH compounds have varying toxicological and environmental persistence properties. When considering risks to human health, current UK designated 'safe' levels (defined as posing a minimal risk to humans) for two of the compounds, benzo[a]pyrene and dibenzo [ah]anthracene, are particularly low and, hence, these compounds are more likely to be found at unacceptable levels possibly requiring remedial works in soils.

In terms of assessing risks to controlled waters, the PAH compounds of most concern are BaP, benzo[b]fluoranthene, benzo[k]fluoranthene, benzo[ghi]pyrene, indeno[123-cd] pyrene, fluoranthene and anthracene. PAH compounds rarely derive from a single source, often with petrogenic (oils and fuels) and pyrogenic (combustion) sources common. There are a number of diagnostic techniques available to identifying the source of the PAH on a site, through comparing the comparative levels of various PAH compounds.

Key Factors in Reuse of Road Planings

Relevant guidance on the reuse of road planings includes CSS ENG/2-97 (Sustainable road maintenance - Reduce, Reuse, Recycle), WRAP (Resource efficiency in highways) and the Specification for Highways Works Series 9002/ 8003. Coal tar compounds and their by-products (e.g. tar oil and pitch) are potentially carcinogenic, and can include very high levels of PAH compounds, some of which have been proven to have carcinogenic effects. The levels of PAH compounds are significantly lower in bitumen and, hence, it is a less hazardous material (PAH compounds commonly pose problems on former industrial and other brownfield development sites).

ESP undertake assessments for clients to assess the levels of contaminants within road planings, provide guidance on re-use options and, if necessary, disposal options. It is good practice (and most cost-efficient) to re-use the planings wherever possible. Depending on the levels of PAH within the planings, re-use options could include inclusion in a hot mix, use as unbound aggregates (subject to a site-specific risk assessment), or as an aggregate in a bitumen bound material such as cold mix asphalt, cement bound material, or hydraulically bound materials. Planings are likely to be classed as 'non hazardous/hazardous waste' and may be costly to dispose of to landfill. Disposal/recycling routes are shown below:

Rising disposal costs and limiting environmental impacts, are driving reduction of waste to landfill.

ESP derive the most appropriate sampling, testing and materials assessment protocol, including options appraisals in line with the Waste Hierarchy. Our detailed understanding of materials and geoenvironmental quality enables design of suitable treatment or disposal options.

*ESP have an in-house CL:AIRE DoWCoP Qualified Person and Environmental Permitting Qualified Staff.

ESP has enabled through the permitting process and directed the establishment of the only hazardous and non-hazardous fixed materials Treatment Facility/Hub in Wales.

✓ = Data Requirement

(http://www.earthsciencepartnership.co.uk/projects/advice-avoiding-disposal-appropriate-reuse-road-planings/)

ΕΝΔΙΑΦΕΡΟΝΤΑ – ΛΟΙΠΑ

Η ιστορία του ISS
Αρχιτεκτονική πέρα από τη Γη

Ο Διεθνής Διαστημικός Σταθμός από το παράθυρο του διαστημοπλοίου «Endeavor» τον Δεκέμβριο του 2011

Πολλά έχουν γραφτεί για τον Διεθνή Διαστημικό Σταθμό (ISS) και τους αστροναύτες του, για τα επιστημονικά πειράματα που διεξάγονται σε αυτόν και τις αποστολές που γίνονται ως εκεί. Ωστόσο, παρά το γεγονός ότι εξάπτει το ενδιαφέρον των επιστημόνων και όσων γοητεύονται από το Διάστημα και τα διαστημικά ταξίδια, ώς τώρα ελάχιστοι έχουν σκεφτεί να τον «εξετάσουν» από την αρχιτεκτονική του σκοπιά.

Αυτό το κενό έρχεται να συμπληρώσει ένα βιβλίο, το «International Space Station, Architecture beyond Earth» («Διεθνής Διαστημικός Σταθμός, Αρχιτεκτονική πέρα από τη Γη»), που θα κυκλοφορήσει την 1η Μαρτίου στη Βρετανία. Ο συγγραφέας του, Ντέιβιντ Νίξον, έχει να πει πολλά από «πρώτο χέρι», αφού είναι ένας από τους ελάχιστους αρχιτέκτονες που έχουν κληθεί να συμμετάσχουν στον σχεδιασμό του ISS, το «θαύμα της σύγχρονης μηχανικής» όπως ο ίδιος τον αποκαλεί.

Κατοικήσιμος δορυφόρος

Ο ISS είναι ένας διαστημικός σταθμός - ή κατοικήσιμος δορυφόρος - ο οποίος σχεδιάστηκε εξαρχής ως «δομοστοιχειωτή κατασκευή». Αποτελεί δηλαδή μια αρθρωτή κατασκευή, η οποία έχει σχεδιαστεί για να συμπληρώνεται, σε βάθος χρόνου και ανάλογα με τις ανάγκες, από αυτοτελείς μονάδες. Με τον τρόπο αυτόν οι αρμόδιοι για τον σχεδιασμό του έκριναν ότι θα μπορούσε να εξυπηρετήσει καλύτερα τον σκοπό του, να χρησιμεύσει δηλαδή ως ένα ερευνητικό εργαστήριο σε συνθήκες μικροβαρύτητας και διαστημικού περιβάλλοντος.

Οι αστροναύτες που διαμένουν σε αυτόν διεξάγουν σε μόνιμη βάση πειράματα -βιολογίας, φυσικής, αστρονομίας, μετεωρολογίας κ.ά.- ενώ εκεί δοκιμάζονται επίσης διάφορα συστήματα και εξοπλισμοί που αναπτύσσουν οι διαστημικές υπηρεσίες για τις μελλοντικές διαστημικές αποστολές τους. Τα περισσότερα δηλαδή τμήματά του αποτελούν εργαστήρια, τα οποία σχεδιάζονται και εξοπλίζονται με βάση το πρόγραμμα των πειραμάτων που θα πρέπει να φιλοξενήσουν.

Η συναρμολόγηση του Διεθνούς Διαστημικού Σταθμού ξεκίνησε τον Νοέμβριο του 1998. Το πρώτο τμήμα του που τέθηκε σε χαμηλή τροχιά γύρω από τη Γη ήταν το ρωσικό Zarya, ακολουθούμενο δύο εβδομάδες αργότερα από το αμερικανικό Unity. Σήμερα αποτελεί τον μεγαλύτερο τεχνητό δορυφόρο που βρίσκεται σε τροχιά γύρω από τον πλανήτη μας: «Πετάει» σε ύψος 330-435 χλμ. και συχνά είναι ορατός με γυμνό μάτι.

Στον κεντρικό σκελετό του εκτός από τα ηλιακά πάνελ, τις κάμερες, τα συστήματα θέρμανσης κ.λπ., είναι πλέον προσαρτημένα 15 τμήματα - κάποια εξ αυτών συνοδεύονται από ρομποτικούς βραχίονες, πλατφόρμες πρόσδεσης και άλλα «αξεσουάρ» - ενώ αναμένεται να ακολουθήσουν ακόμη πέντε. Η αποστολή του Bigelow Expandable Activity Module (BEAM) της NASA, το οποίο θα είναι το πρώτο «φουσκωτό» τμήμα που προσαρτάται ποτέ σε διαστημικό σταθμό, αναμένεται να προστεθεί τον ερχόμενο Απρίλιο ενώ η αποστολή του ρωσικού Nauka, το οποίο θα φέρει και τον Ευρωπαϊκό Ρομποτικό Βραχίονα, έχει προγραμματιστεί για τον Φεβρουάριο του 2017.

Θαύμα της μηχανικής

Το «International Space Station, Architecture beyond Earth» αποτελεί, όπως τονίζει ο εκδοτικός οίκος Circa Press, την πρώτη ολοκληρωμένη αφήγηση τόσο της σύλληψης και του σχεδιασμού του σταθμού όσο και της κατασκευής των τμημάτων του και της συναρμολόγησής τους στο Διάστημα. Καθώς πρόκειται πραγματικά για ένα μοναδικό δείγμα της μηχανικής, της τεχνολογίας και της αρχιτεκτονικής, οι εκδότες θεωρούν ότι το περιεχόμενό του μπορεί να έχει απήχηση και στο ευρύτερο κοινό πέρα από τους «στενούς» φίλους του Διαστήματος.

Για τους τελευταίους πάντως το όνομα του Ντέιβιντ Νίξον αποτελεί ένα επιπλέον κίνητρο. Ο «διαστημικός αρχιτέκτονας», όπως τον αποκαλούν, είναι ένας εκ των ιδρυτών της Future Systems και είναι γνωστός για τη σχεδιαστική συνεισφορά του στη διαστημική εξερεύνηση.

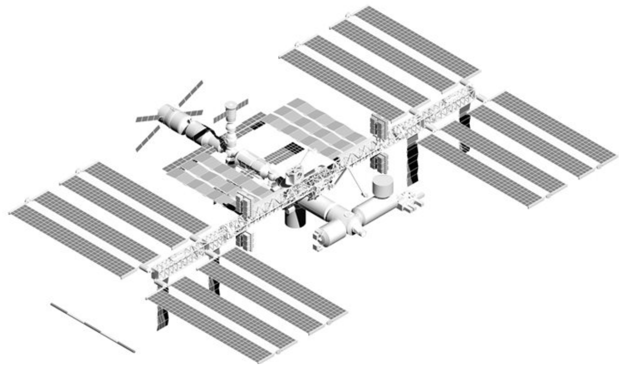

Ισομετρικό σχέδιο του Διεθνούς Διαστημικού Σταθμού, ολοκληρωμένου, από τον Ντέιβιντ Νίξον

«Μία από τις χαρές των μεγάλων έργων της αρχιτεκτονικής και της μηχανικής είναι ότι μπορεί κάποιος να τα επισκεφθεί» δήλωσε σε δελτίο Τύπου ο κ. Νίξον με αφορμή την επικείμενη κυκλοφορία του βιβλίου.

«Μπορεί κάποιος να διασχίσει με το αυτοκίνητο τη γέφυρα Γκόλντεν Γκέιτ, να ανέβει στον Πύργο του Αϊφελ, να περπατήσει στο Κολοσσαίο ή να απολαύσει μια παράσταση στην Όπερα του Σίδνεϊ. Αυτό δεν ισχύει για τον Διεθνή Διαστημικό Σταθμό. Μόνο μερικοί ειδικά εκπαιδευμένοι αστροναύτες και κοσμοναύτες μπορούν να τον δουν. Οι υπόλοιποι πρέπει να αρκεστούμε σε βίντεο και φωτογραφίες για να πάρουμε μια αίσθηση του πώς είναι από κοντά. Για τον λόγο αυτόν προκαλεί μεγάλη έκπληξη το γεγονός ότι τόσο λίγα έχουν γραφτεί για ένα έργο το οποίο μπορεί να θεωρηθεί το αριστούργημα της μηχανικής και της οικοδομικής της σύγχρονης εποχής. Ελπίζω το βιβλίο αυτό να ξεκινήσει τη συμπλήρωση αυτού του κενού».

(Λαλίνα Φαφούτη / Βήμα Science Newsroom ΔΟΛ, 23 Feb. 2016, http://www.tovima.gr/science/article/?aid=778865)

Viaduc de Millau

343 mètres! Plus haut que la tour Eiffel, un prodige de construction...

Les ouvriers ne doivent pas craindre le vertige, des as de la voltige !

Regardez!...

ꕥ ꕥ

Beijing-Shanghai high-speed rail train

The **Beijing–Shanghai High-Speed Railway** (or **Jinghu High-Speed Railway** from its Chinese name) is a 1,318-kilometre long high-speed railway that connects two major economic zones in the People's Republic of China, the Bohai Economic Rim and the Yangtze River Delta. Construction began on April 18, 2008, and a ceremony to mark the completion of track laying was held on November 15, 2010. The line opened to the public for commercial service on June 30, 2011. This rail line is the world's longest high-speed line ever constructed in a single phase. Under former Minister of Railways Liu Zhijun, the railway line was the first one designed for a maximum speed of 380 km/h in commercial operations. The non-stop train from Beijing South to Shanghai Hongqiao was expected to finish the 1,305 kilometres journey in 3 hours and 58 minutes, averaging 329 kilometres per hour, making it the fastest scheduled train in the world, compared to 9 hours and 49 minutes on the fastest trains running on the parallel conventional railway. However, following Liu Zhijun's dismissal in February 2011, several major changes were announced. First, trains would be slowed to a maximum speed of 300 km/h, reducing operating costs. At this speed, the fastest trains would take 4 hours and 48 minutes to travel from Beijing South to Shanghai Hongqiao, making one stop at Nanjing South. Additionally, a slower class of trains running at 250 km/h would be operated, making more stops and charging lower fares.

The railway line has some of the longest bridges in the world. They include:

- Danyang–Kunshan Grand Bridge - longest bridge in the world.

- Tianjin Grand Bridge - second longest bridge in the world.

- Beijing Grand Bridge (μήκους 48 km!!!
- Cangzhou–Dezhou Grand Bridge
- Nanjing Qinhuai River Bridge
- Zhenjiang Beijing–Hangzhou Canal Bridge

First day in service

Tickets were put on sale at 09:00 on June 24, 2011, and sold out within an hour. To compete with the new train service, airlines slashed the cost of flights between Beijing and Shanghai by up to 65%. Economy air fares between Beijing and Shanghai fell by 52%.

On June 30, 2011 the official carrier of the first riders of the Beijing-Shanghai high-speed rail train pulled out from the Beijing South Railway Station, bound for Shanghai.

Through the Beijing South Third Ring Road.

The crew to board the first Beijing-Shanghai high-speed rail train.

Put into trial operation of trains is divided into first-class car, second-class cars, dining cars, business cars and VIP tourist area.

To meet the special requirements of passengers, there are dedicated disabled riding area, wheelchair accessible bathrooms and corridors.

ΗΛΕΚΤΡΟΝΙΚΑ ΠΕΡΙΟΔΙΚΑ

www.geoengineer.org

Κυκλοφόρησε το Τεύχος #131 του **Newsletter του Geoengineer.org** (Φεβρουαρίου 2016) με πολλές χρήσιμες πληροφορίες για όλα τα θέματα της γεωμηχανικής. Υπενθυμίζεται ότι το Newsletter εκδίδεται από τον συνάδελφο και μέλος της ΕΕΕΕΓΜ Δημήτρη Ζέκκο (secretariat@geoengineer.org).

Newsletter #23 - February 2016

www.itacet.org/newsletter/nl_detail.php?no_nl=23

Κυκλοφόρησε το Τεύχος 23 (Φεβρουαρίου 2016) με τα παρακάτω περιεχόμενα:

- President's Address, Eng. Abdullah bin Abdulrahman Al-Muqbel
- Special Event: Two Training Courses at the WTC 2016 in San Francisco
- Three new programs in our Portfolio
- Coming Soon: Waterproofing. Santiago, Chile. 16-17 March 2016
- Next Events in preparation

  TUNNEL DESIGN. Bhutan, Thimphu, 30-31 May 2016.

  IMMERSED TUNNELS. Amsterdam, Nederland, 06-07 Septembre 2016.

  CONTRACTS and RISKS. Nepal, Kathmandu, October 2016.
- Events Report: "Tunnelling and Lanslides" and "Rockfall and Protection Techniques" in Riyadh (KSA)
- ITACET Committee special lecture by Prof. Robert Galler
- Collaboration with ITA Endorsed Master Course program of Polytechnic University Turin (I)
- News from our Sponsored Master Students

ΕΚΤΕΛΕΣΤΙΚΗ ΕΠΙΤΡΟΠΗ ΕΕΕΕΓΜ (2015 – 2018)

ΕΕΕΕΓΜ
Τομέας Γεωτεχνικής
ΣΧΟΛΗ ΠΟΛΙΤΙΚΩΝ ΜΗΧΑΝΙΚΩΝ
ΕΘΝΙΚΟΥ ΜΕΤΣΟΒΙΟΥ ΠΟΛΥΤΕΧΝΕΙΟΥ
Πολυτεχνειούπολη Ζωγράφου
15780 ΖΩΓΡΑΦΟΥ

Τηλ. 210.7723434
Τοτ. 210.7723428
Ηλ-Δι. secretariat@hssmge.gr ,
geotech@central.ntua.gr
Ιστοσελίδα www.hssmge.org (υπό κατασκευή)

«ΤΑ ΝΕΑ ΤΗΣ ΕΕΕΕΓΜ» Εκδότης: Χρήστος Τσατσανίφος, τηλ. 210.6929484, τοτ. 210.6928137, ηλ-δι. ctsatsanifos@pangaea.gr, editor@hssmge.gr, info@pangaea.gr

«ΤΑ ΝΕΑ ΤΗΣ ΕΕΕΕΓΜ» «αναρτώνται» και στην ιστοσελίδα www.hssmge.gr